

Offshore-onshore resistivity imaging of freshwater using a controlled-source electromagnetic method: A feasibility study

Keiichi Ishizu¹ and Yasuo Ogawa¹

ABSTRACT

Coastal freshwater provides a water source for more than one billion people living in coastal regions. For sustainable groundwater management in coastal areas, an understanding of freshwater distribution is necessary. Freshwater distribution in a coastal area can extend across the shoreline and into the offshore region. Offshore-onshore mapping of freshwater helps us to gain a comprehensive understanding of the freshwater distribution in coastal areas. Resistivity imaging using electromagnetic methods has been used to reveal the freshwater distribution in coastal areas because electrical resistivity in these settings is primarily controlled by porosity and porewater salinity. We have considered a controlled-source electromagnetic (CSEM) method for offshore-onshore resistivity imaging of freshwater at a depth range of 0–500 m below the seafloor. Our CSEM method is novel in considering an array of onshore-offshore electromagnetic receivers with onshore electric dipole transmitters. We have conducted a feasibility study to investigate the ability of the CSEM method for offshore-onshore resistivity imaging of freshwater in a coastal area. The test results indicate that the method could image the resistivity distribution of freshwater located at a depth of 500 m below the seafloor. Our model study also indicates that the offshore-onshore CSEM method can detect offshore aquifers up to 5 km from the shoreline. These numerical test results imply that our CSEM method is a promising technique for offshore-onshore resistivity imaging of freshwater in coastal areas.

INTRODUCTION

Coastal freshwater is essential to water resources, providing a water source for more than one billion people living in coastal

regions (Post, 2005). For sustainable groundwater management in coastal areas, it is necessary to understand the coastal freshwater distribution, which can extend across the shoreline and into the offshore region (Johnston, 1983). The offshore-onshore mapping of freshwater can, therefore, help us to gain a comprehensive understanding of the freshwater distribution in coastal areas. In coastal areas of Japan, carbon capture and storage projects are ongoing (Sawada et al., 2018); they require freshwater distribution maps because the fluid migration process is critical for their application (Gaus, 2010).

The distribution of electrical resistivity provides a useful constraint for the distribution and salinity of fluid. In coastal areas, the bulk resistivity primarily depends on porosity and porewater salinity and temperature (Archie, 1942; Revil et al., 1998). Using Archie's law, porewater salinity can be determined by the bulk resistivity under an assumed porosity. Based on onshore well-logging data near the shoreline, Ueda et al. (2014) find that a high bulk resistivity (20 ohm-m) corresponded to sediments with low-salinity porewater, whereas a low bulk resistivity (1 ohm-m) corresponded to sediments with high-salinity porewater. The electromagnetic method, which can remotely reveal the spatial distribution of resistivity, is suitable for investigating the distribution and salinity of fluid below the ground and seafloor due to the contrasting resistivity values.

Electromagnetic and electric geophysical methods have been used to map the spatial distribution of resistivity in coastal areas (Dimova et al., 2012; Binley et al., 2015). Electric resistivity tomography provides resistivity mapping by deploying electrodes from the landward side to the seaward side with a shallow exploration depth of approximately 50 m below the seafloor (Hermans and Paepen, 2020). The airborne transient electromagnetic (TEM) method can be used to quickly investigate the extensive resistivity distribution in coastal areas; however, its penetration depth is strongly limited by the existence of the conductive sea layer (Ito et al., 2011; Pedersen et al., 2017). Magnetotelluric (MT) methods have been used to map offshore-onshore resistivity structures over a

Manuscript received by the Editor 12 December 2020; revised manuscript received 12 May 2021; published ahead of production 24 August 2021; published online 30 September 2021.

¹Tokyo Institute of Technology, Volcanic Fluid Research Center, S5-13, 2-12-1 Ookayama, Meguro, Tokyo 152-8551, Japan. E-mail: ishizu.k.ab@m.titech.ac.jp, ishizu.keiichi.n30@kyoto-u.jp (corresponding author); oga@ksvo.titech.ac.jp.

© 2021 Society of Exploration Geophysicists. All rights reserved.

deeper range (Mitsuhata et al., 2006; Ueda et al., 2014; Suzuki et al., 2017). However, the MT method is insensitive to thin resistive structures of freshwater compared with controlled-source electromagnetic (CSEM) methods (Gustafson et al., 2019). In this study, we focus on a CSEM method to overcome the limited exploration depth and mapping ability of thin resistive freshwater in a coastal area.

To explore various targets (e.g., hydrocarbon, gas hydrate, metal deposits, and freshwater), previous studies have used CSEM methods on land (Wirianto et al., 2010; Grayver et al., 2014; Strack, 2014; Tietze et al., 2015; Streich, 2016; Schaller et al., 2017; Malovichko et al., 2019) and in marine environments (Eidesmo et al., 2002; Evans, 2007; Plessix and Mulder, 2008; Commer and Newman, 2009; Schwabenberg et al., 2010; Key, 2012; Zhdanov et al., 2014; Haroon et al., 2017, 2018; Blatter et al., 2019; Constable et al., 2019; Gustafson et al., 2019; Johansen et al., 2019; Lippert and Tezkan, 2020; Micallef et al., 2020). Although CSEM methods are sensitive to conductors and resistors, a particularly important feature is their higher sensitivity to thin buried resistors. By using the sensitivity to thin resistive targets, CSEM methods have been used to image offshore freshwater (Evans, 2007; Blatter et al., 2019; Gustafson et al., 2019; Attias et al., 2020; Lippert and Tezkan, 2020; Micallef et al., 2020).

The present study's target is the freshwater distribution from the seaward side to the landward side in a coastal area. We propose a frequency-domain CSEM method with onshore transmitters and amphibious receivers for offshore-onshore resistivity imaging of freshwater, and we present a feasibility test to demonstrate its effectiveness through forward modeling and inversion. Our CSEM method is novel in considering an array of amphibious electromagnetic receivers with onshore electric dipole transmitters. First, we describe the CSEM method and its 3D forward modeling and inversion. Then, a conceptual freshwater model in a coastal area is presented for the feasibility test, and we conduct the forward-modeling test using the conceptual model. Finally, we investigate the 3D imaging ability of the CSEM method by applying the inversion to synthetic data generated from the conceptual model.

METHODS

CSEM method for offshore-onshore resistivity imaging of freshwater

The CSEM method uses artificial electromagnetic fields to infer the subsurface electrical resistivity structure (Constable, 2010;

Streich, 2016). Many different sources and receiver configurations have been proposed for CSEM methods. The electric dipole-dipole CSEM method is a specific variation sensitive to thin resistive layers, whereas the magnetic dipole-dipole CSEM methods are used for mineral prospecting of conductive bodies (Constable, 2013; Streich, 2016). Notably, the marine frequency-domain CSEM method using electric dipole-dipole configuration has become a well-established geophysical tool for the imaging of hydrocarbons in the deep sea (Constable, 2010). We focus on a configuration of electric dipole transmitters and electromagnetic receivers because this configuration is sensitive to thin resistive layers of freshwater.

As mentioned in the "Introduction" section, CSEM methods have been used in land and marine environments to explore various targets. For the typical marine CSEM method, the transmitter dipole is towed from the ship to 20–50 m above the seafloor, where the seafloor receivers subsequently record the resultant electromagnetic fields (Eidesmo et al., 2002; Plessix and Mulder, 2008; Commer and Newman, 2009; Constable, 2010; Key, 2012; Mittet and Morten, 2013). Marine CSEM receivers can also be towed behind the survey vessel (Sherman et al., 2017; Gustafson et al., 2019; Attias et al., 2020). Land CSEM methods use transmitters and receivers on the ground surface (Grayver et al., 2014; Strack, 2014). The presence of a conductive seawater layer has a profound influence on the electromagnetic field propagation and so marks a fundamental difference between terrestrial and marine approaches to surveying.

Freshwater exploration on the seafloor has been undertaken using CSEM methods based on the sea-surface towed configuration (Blatter et al., 2019; Gustafson et al., 2019) and seafloor deployed transmitter and receiver arrays (Evans et al., 2007; Haroon et al., 2017; Lippert and Tezkan, 2020; Micallef et al., 2020). Given that our target is the freshwater distribution from the seaward side to the landward side in a coastal area, we propose a new CSEM method that consists of onshore electric dipole transmitters and amphibious electromagnetic receivers (Figure 1) to obtain offshore-onshore resistivity imaging. This CSEM method is a combination of offshore and onshore CSEM methods, and it actually resembles an onshore CSEM method with a configuration of the surface transmitter and receivers buried below the ground. We conducted numerical tests using forward modeling and inversion to demonstrate the effectiveness of the CSEM method for offshore-onshore resistivity imaging of freshwater. The next section briefly describes the 3D forward modeling and inversion processes.

3D CSEM forward modeling and inversion

The 3D CSEM forward modeling method used the finite-difference method (FDM) combined with a scattered field approach. In the scattered field approach, the electric and magnetic fields are split into primary and secondary parts as follows:

$$\mathbf{E} = \mathbf{E}^p + \mathbf{E}^s, \quad (1)$$

$$\mathbf{H} = \mathbf{H}^p + \mathbf{H}^s, \quad (2)$$

where \mathbf{E}^p represents the primary electric field, \mathbf{E}^s denotes the secondary electric field, \mathbf{H}^p signifies the primary magnetic field, and \mathbf{H}^s represents the secondary magnetic field. Splitting into primary and secondary fields excludes source-point singularities from numerical

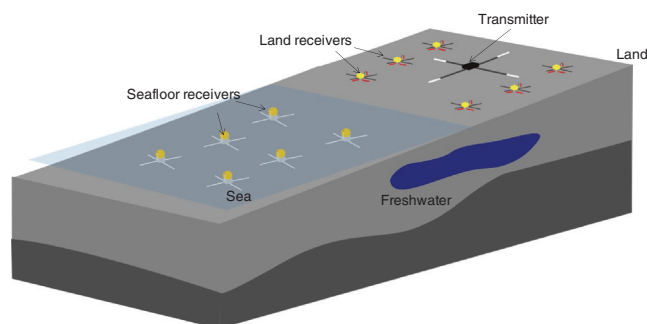


Figure 1. Schematic diagram of a CSEM method for offshore-onshore resistivity imaging of freshwater in a coastal area. Our study examines a CSEM method that involves onshore transmitters and onshore-offshore receivers.

computations (Newman and Alumbaugh, 1997; Weiss and Constable, 2006). Primary fields are analytically calculated by solving the Hankel transform in layered earth conductivity (Key, 2009). The transmitter used in this study was a point source dipole.

Using the calculated primary field, we solved the vector Helmholtz equation for the secondary electric field as follows:

$$-\nabla \times \nabla \times \mathbf{E}^s + i\omega\mu\sigma\mathbf{E}^s + i\omega\mu(\sigma - \sigma^p)\mathbf{E}^p = 0, \quad (3)$$

where ω denotes the angular frequency of the field assuming the time dependence of the form $e^{-i\omega t}$, μ is the magnetic permeability, σ is the conductivity, and σ^p represents the background layered earth conductivity for the primary field computation. We applied FDM with a staggered grid to equation 3, thus resulting in a linear system:

$$\mathbf{A}\mathbf{E}^s = \mathbf{b}, \quad (4)$$

where \mathbf{A} is complex, sparse, and symmetric positive definite and \mathbf{b} is a vector including the primary field information and the Dirichlet boundary condition of the secondary electric field. PARDISO, a multicore parallel sparse direct solver, was used to solve the linear system. Direct solvers are numerically robust, especially for low-frequency electromagnetic difficulties (Oldenburg et al., 2013). The computed secondary field was added to the primary field to obtain the total field.

To convert the CSEM data to resistivity structures, we use a 3D inversion code based on the data-space Occam algorithm (Siripunvaraporn and Egbert, 2000). The Occam inversion algorithm seeks the model with the minimum norm at an appropriate misfit level by automatically adjusting the regularization parameter (Constable et al., 1987). The data-space approach can reduce the computation costs of memory and CPU time if the data number N is less than the model number M (Siripunvaraporn and Egbert, 2000). For the 3D CSEM method considered here, N is much lower than M , thus reducing the computational costs.

The regularized inverse problem seeks to minimize the functional as follows:

$$U = (\mathbf{m} - \mathbf{m}_0)^T \mathbf{C}_m^{-1} (\mathbf{m} - \mathbf{m}_0) + \lambda^{-1} \{ (\mathbf{d} - \mathbf{F}[\mathbf{m}])^T \mathbf{C}_d^{-1} (\mathbf{d} - \mathbf{F}[\mathbf{m}]) - \chi_*^2 \}, \quad (5)$$

where \mathbf{m} is a vector $\log_{10} \sigma$, \mathbf{m}_0 denotes a prior model, \mathbf{d} represents the observed data, $\mathbf{F}[\mathbf{m}]$ signifies the forward-modeling response, \mathbf{C}_m is the model covariance, \mathbf{C}_d is a data covariance matrix, χ_* represents the desired level of misfit, and λ^{-1} is a Lagrange multiplier. To minimize U in equation 5, we take the derivative with respect to the model and set it to zero. Nonlinearity in CSEM methods means that the resulting equation is solved iteratively by creating a sequence of models, each of which gradually provides a better fit to the data. After linearizing an initial model (\mathbf{m}_k), the next model, \mathbf{m}_{k+1} , is expressed by

$$\mathbf{m}_{k+1} - \mathbf{m}_0 = \mathbf{C}_m \mathbf{J}_k^T \boldsymbol{\beta}_{k+1}, \quad (6)$$

where $\boldsymbol{\beta}_{k+1}$ is an unknown expansion coefficient vector of the basis functions $\mathbf{C}_{mJ_k^T}$. The vector $\boldsymbol{\beta}_{k+1}$ is obtained by solving

$$(\lambda \mathbf{C}_d + \mathbf{J}_k \mathbf{C}_m \mathbf{J}_k^T) \boldsymbol{\beta}_{k+1} = \hat{\mathbf{d}}_k, \quad (7)$$

where

$$\hat{\mathbf{d}}_k = \mathbf{d} - \mathbf{F}[\mathbf{m}_k] + \mathbf{J}_k (\mathbf{m}_k - \mathbf{m}_0). \quad (8)$$

Therefore, \mathbf{J}_k is the sensitivity matrix of $N \times M$ at \mathbf{m}_k . We solved the dense and symmetric $N \times N$ matrix in equation 7 using a parallel direct solver of “dposv” from MKL LAPACK using the Cholesky decomposition. The model update iterations are continued until the target misfit χ_* has been reached. The regularization term \mathbf{C}_m^{-1} is defined as the first derivative roughness penalty.

RESULTS

We conducted numerical tests to investigate the effectiveness of the CSEM method for offshore-onshore resistivity imaging of freshwater in a coastal area. First, a conceptual resistivity model for the feasibility test is presented. Then, we conduct the detectability test using forward modeling. The points mainly studied in the test are the effects of transmitter-receiver geometries, transmitting frequencies, different sea depths, and different freshwater burial depths on detectability. The 3D imaging ability of the CSEM method is demonstrated by applying the inversion to synthetic data generated from the conceptual model. We also compare the imaging ability of the CSEM and MT inversion using synthetic data.

Conceptual model in a coastal zone

A conceptual offshore-onshore resistivity model resembles a model obtained by the 2D inversion of MT data in a coastal area, Hokkaido, north Japan, as shown in Ueda et al. (2014; Figure 7). The MT inversion imaged freshwater zones with a resistivity of 20 ohm-m, and these freshwater zones have been confirmed by on-shore well-logging data (Ueda et al., 2014). The conceptual model includes 1 ohm-m sediments, 0.3 ohm-m seawater, and a 20 ohm-m resistive anomaly simulating a freshwater zone with dimensions of 2000 m (width) \times 3000 m (length) \times 100 m (height) (Figure 2). An

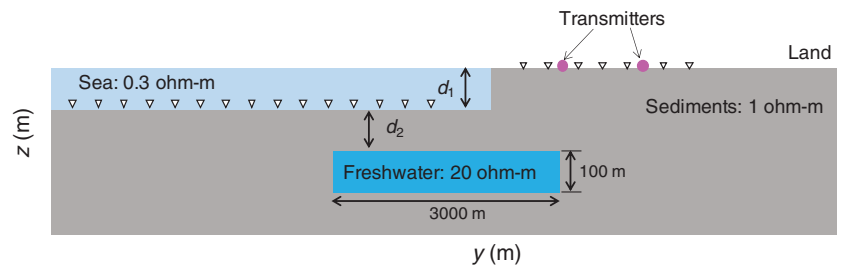


Figure 2. Synthetic model to demonstrate the effectiveness of a CSEM survey for the offshore-onshore resistivity imaging of freshwater. The model includes air, sea, sediments, and a 20 ohm-m freshwater reservoir (dimensions: 2000 m [width] \times 3000 m [length] \times 100 m [height]) embedded into the sediment. The terms d_1 and d_2 denote the sea depth and burial depth of the target freshwater, respectively. The circles and triangles indicate the transmitter and receiver positions, respectively. The shoreline followed the x -direction at $y = 0$ m.

air layer with resistivity of 10^8 ohm-m is present at the top of the model. For the later detectability test, the sea depth and the burial depth of the target freshwater were denoted by d_1 and d_2 , respectively. The 3D view of the resistivity model with $d_1 = 30$ m and $d_2 = 300$ m is displayed in Figure 3.

Three transmitter sites were located at $(x, y, z) = (0 \text{ m}, 1000 \text{ m}, 0 \text{ m})$, $(0 \text{ m}, 2000 \text{ m}, 0 \text{ m})$, and $(0 \text{ m}, 3000 \text{ m}, 0 \text{ m})$ on land, each of which included two horizontal electric dipoles (HEDs) oriented along the x - and y -directions. Receivers were deployed on the seafloor and ground at 500 m intervals from $y = -5000$ to 3000 m at three profiles of $x = -1500, 0$, and 1500 m. The shoreline followed the x -direction at $y = 0$ m. The electromagnetic components observed in the inline array (the transmitter pointing toward the y -direction and the receivers positioned along the y -axis) were E_y , E_z , and H_x . The components in the broadside array (the transmitter pointing toward the x -direction and the receivers positioned along the y -axis) were E_x , H_y , and H_z . We normalized the \mathbf{E} (V/m) and \mathbf{H} (A/m) values recorded at the receivers using the source dipole

moment (Am). The units of the \mathbf{E} and \mathbf{H} amplitudes are V/Am^2 and $1/\text{m}^2$, respectively.

Detectability test using forward modeling

We conducted a numerical test using forward modeling to investigate the ability of the proposed CSEM method to detect the freshwater zone. This test used the conceptual resistivity model, which included freshwater (Figure 2). To investigate the detectability of the target freshwater, we used the normalized amplitude (R^0):

$$R^0 = \frac{|R^a|}{|R^b|}, \quad (9)$$

where R^a is the CSEM response with a target anomaly of freshwater and R^b is the CSEM response without an anomaly. The R^0 value provides a useful indicator of a target structure's detectability (Swidinsky et al., 2013), where an R^0 value of one indicates no detectability.

The forward-modeling calculation of the CSEM responses was performed on a computer (@Xeon 3.10 GHz Gold 6254 CPU; Intel Corp.) with 3 TB of RAM. A computation grid consisted of $56 \times 133 \times 95$ cells, including several boundary cells. For the horizontal cells, a 100 m grid was used. We appended the boundary cells at each side, growing at a stretching factor of 2.0. For the vertical grid, the finest grid of 5 m was used near the transmitter, and the grid size increased gradually with the increasing distance from the transmitters. Before conducting the test, we compared the forward-modeling responses with the analytical solutions in the 1D resistivity models. The comparisons showed that the forward modeling could produce sufficiently accurate responses for the 1D resistivity models.

CSEM responses depend on earth resistivity structures, transmitter-receiver geometries, and transmitting frequencies. Understanding the effective transmitter-receiver geometries and transmitting frequencies for imaging target structures is helpful for an efficient data acquisition in the field. First, we conducted a test on the effective transmitter-receiver geometries and transmitting frequencies. We considered the 3D resistivity model shown in Figure 3, which corresponds to a model of Figure 2 with $d_1 = 30$ m and $d_2 = 300$ m. We generated CSEM responses for the three onshore transmitter positions at $(x, y, z) = (0 \text{ m}, 1000 \text{ m}, 0 \text{ m})$, $(0 \text{ m}, 2000 \text{ m}, 0 \text{ m})$, and $(0 \text{ m}, 3000 \text{ m}, 0 \text{ m})$ using forward modeling. The transmitters used a y -direction HED, and the receiver line was along the y -direction at $x = 0$ m. The transmitting frequencies were 0.01, 0.1, and 1.0 Hz.

The inline E_y from a y -direction transmitter dipole at $(0 \text{ m}, 1000 \text{ m}, 0 \text{ m})$ showed a clear detectability of the target freshwater (Figure 4a and 4c). The 20 ohm-m resistive freshwater increased the E_y amplitude on the receivers. The maximum R^0 values for 0.01, 0.1, and 1.0 Hz were 2.2, 2.6, and 2.9, respectively. The higher frequencies obtained a greater detectability for the transmitter dipole at $(0 \text{ m}, 1000 \text{ m}, 0 \text{ m})$. The seafloor receiver at $y = -500$ m recorded a maximum R^0 value of 2.9 for 1.0 Hz. The maximum R^0 values for 0.1 and 0.01 Hz were observed at a seafloor receiver at $y = -2000$ m. The seafloor receiver at $y = -5000$ m from the freshwater recorded few effects of the freshwater anomaly at all three frequencies. The R^0 values for the onshore receivers were much smaller than those of the seafloor receivers. We also calculated CSEM data at a frequency of 10 Hz. The maximum R^0 values for 10 Hz were 1.1. The 10 Hz

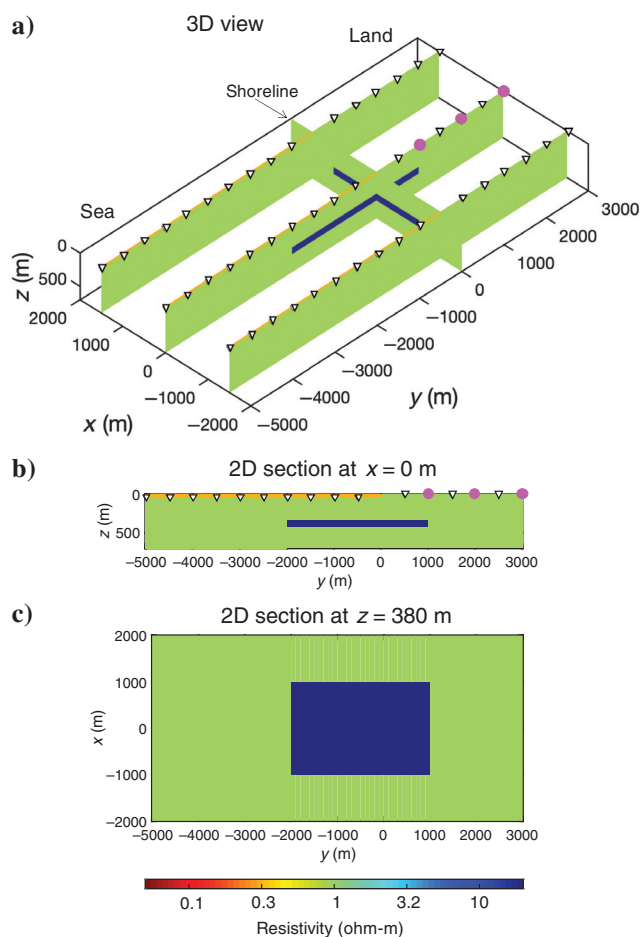


Figure 3. (a) The 3D view of the synthetic model shown in Figure 2 with the sea depth (d_1) set to 30 m and the burial depth of freshwater (d_2) set to 300 m. This model includes air, sea, sediments, and a 20 ohm-m freshwater reservoir (dimensions: 2000 m [width] \times 3000 m [length] \times 100 m [height]) embedded into 1 ohm-m sediments (top at $z = 330$ m). (b and c) The 2D sections of the model at $x = 0$ m and $z = 380$ m, respectively. The circles and triangles show the transmitter and receiver positions, respectively. The shoreline followed the x -direction at $y = 0$ m.

data obtained much lower detectability than the 1 Hz for this model setting.

The E_y responses of the transmitter dipole at (0 m, 2000 m, 0 m) exhibited smaller detectability than those of the transmitter dipole at (0 m, 1000 m, 0 m) for all three frequencies (Figure 4b and 4d). The maximum R^0 values for 0.01, 0.1, and 1.0 Hz were 1.3, 1.4, and 1.1, respectively; hence, the highest R^0 value was observed at 0.1 Hz. The seafloor receiver at $y = -1500$ m observed a maximum R^0 value of 1.4 at a frequency of 0.1 Hz (Figure 4d). The pattern of detectability for the R^0 at 1.0 Hz differed to the patterns at 0.01 and 0.1 Hz. The observed inline E_y at 0.01 and 0.1 Hz had R^0 values of >1.0 , thus indicating that the existence of freshwater increased the amplitude. However, the response at 1.0 Hz had an R^0 value of <1 at the seafloor receivers from $y = -2500$ to -500 m. The E_y responses of the transmitter dipole at (0 m, 3000 m, 0 m) had a smaller detectability than those of the transmitter dipoles at (0 m, 1000 m, 0 m) and (0 m, 2000 m, 0 m). The maximum R^0 value was 1.1 at 0.1 Hz.

The receivers recorded the phase information of electromagnetic fields as well as the amplitude. The phases and their difference for inline E_y responses generated from y -direction transmitter dipoles at (0 m, 1000 m, 0 m) and (0 m, 2000 m, 0 m) are shown in Figure 5. The maximum phase difference values for the transmitter dipole at (0 m, 1000 m, 0 m) for 0.01, 0.1, and 1.0 Hz were 0.0° , 10.0° , and 55.8° , respectively. The seafloor receiver at $y = -1500$ m exhibited the largest phase difference of 55.8° at 1.0 Hz (Figure 5c). The peak value of the phase difference for the transmitter dipole at (0 m, 2000 m, 0 m) was 11.7° at 1.0 Hz (Figure 5d). The E_y phase difference generated from the transmitter dipole at (0 m, 2000 m, 0 m) was smaller than that at (0 m, 1000 m, 0 m). A similar result was also observed for the amplitude data. The phase difference at 0.01 Hz was close to zero for all receivers of the two transmitters. Inductive attenuation of the electromagnetic field caused the observed phase shift. The process of inductive attenuation and phase shift occurs when the skin depths are comparable to the distance over which the electromagnetic energy has traveled (Constable, 2010).

The other electromagnetic components of E_z and H_x exist in the inline geometry. The usefulness of these components has been demonstrated by numerical tests (Um and Alumbaugh, 2007; Mittet and Morten, 2013) and field data (Constable et al., 2019). We considered E_z and H_x from a y -direction transmitter dipole at (0 m, 1000 m, 0 m). The onshore measurement of E_z was conducted at 0.01 m below the ground surface, and seafloor receivers measured E_z at 0.01 m above the seafloor. Freshwater increased the observed E_z amplitude on the seafloor and land (Figure 6a and 6c). The E_z responses were not smoothly distributed for the transmitter-receiver offset. The maximum R^0 values for 0.01, 0.1, and 1.0 Hz were 14.5, 17.1, and 28.4, respectively. Two peaks were observed at $y = -2500$ m on the

seaward side and at $y = 3000$ m on the landward side. The highest R^0 value of 28.4 at 1.0 Hz was observed at $y = 3000$ m on the landward side. The amplitude of H_x was smaller with resistive freshwater (Figure 6b and 6d). The minimum R^0 values for 0.01, 0.1, and 1.0 Hz were 0.70, 0.68, and 0.66, respectively. The R^0 distribution patterns were similar among the three frequencies. The lowest R^0 values were observed at $y = -500$ m on the seafloor for all three frequencies. In addition, E_z had the highest R^0 value among the inline components of E_y , E_z , and H_x . We note that the higher detectability of E_z in comparison with E_y did not necessarily correspond to a higher resolution (Key, 2012).

The broadside component of E_x generated from an x -direction HED primarily uses the horizontal current. To fully characterize the electromagnetic field responses in a 3D situation, the electromagnetic field must be recorded for at least two different source polarizations (Caldwell et al., 2002). The broadside E_x observed a higher amplitude with a resistive target structure (Figure 7). The maximum R^0 values for 0.01, 0.1, and 1.0 Hz were 1.4, 1.3, and 1.2, respectively. The seafloor receiver at $y = -500$ m near the shoreline observed the highest R^0 values for all three frequencies. The R^0 values were smoothly distributed for the transmitter-receiver offset. The peak R^0 value of E_x was much lower than that of the inline E_y . Model studies of onshore CSEM methods for

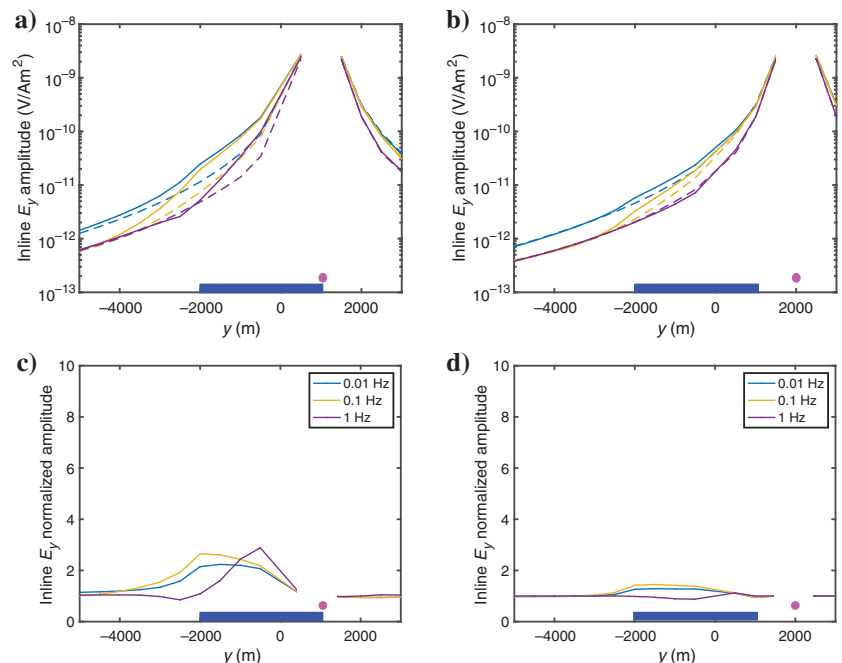


Figure 4. Inline E_y amplitude and normalized amplitude (R^0) for different transmitter positions for the model shown in Figure 3, which corresponds to that in Figure 2 with the sea depth (d_1) set to 30 m and the burial depth of freshwater (d_2) set to 300 m. The transmitters use a y -direction HED. Showing the E_y amplitude for the transmitter at (a) $(x, y, z) = (0 \text{ m}, 1000 \text{ m}, 0 \text{ m})$ and (b) $(0 \text{ m}, 2000 \text{ m}, 0 \text{ m})$ as a function of the receiver along the y -direction at $x = 0$ m. The solid and dashed lines present the response with (R^a) and without (R^b) the freshwater anomaly, respectively. The E_y normalized amplitude (R^0) for the transmitter at (c) $(0 \text{ m}, 1000 \text{ m}, 0 \text{ m})$ and (d) $(0 \text{ m}, 2000 \text{ m}, 0 \text{ m})$. The blue, yellow, and purple lines show the responses at frequencies of 0.01, 0.1, and 1.0 Hz, respectively. The magenta circles and blue rectangles indicate the transmitter position and horizontal position of freshwater, respectively. The shoreline followed the x -direction at $y = 0$ m.

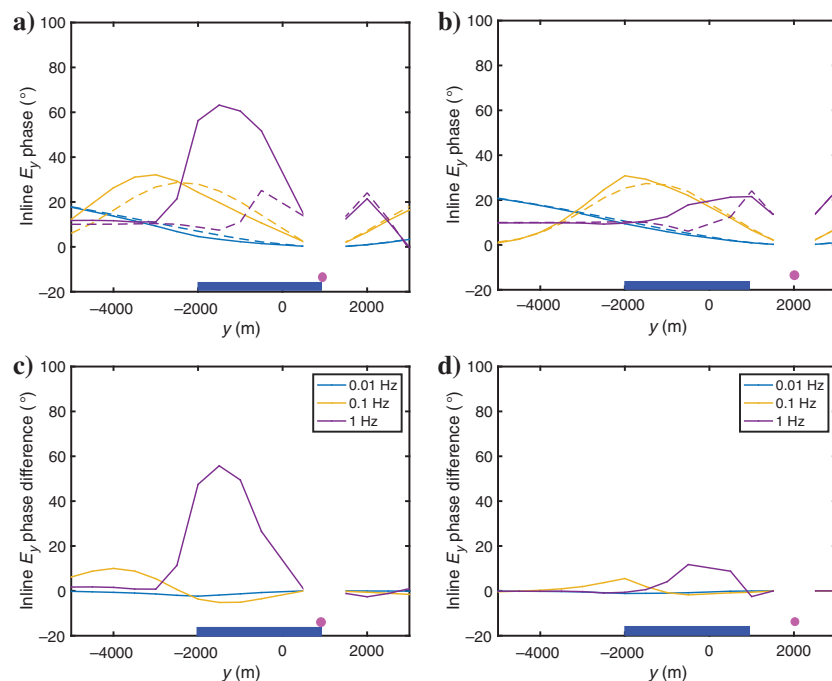


Figure 5. The same as Figure 4 except that inline E_y phase and phase difference are plotted. The E_y phase for transmitter at (a) $(x, y, z) = (0, 1000, 0)$ m and (b) $(0, 2000, 0)$ m, and E_y phase difference for the transmitter at (c) $(0, 1000, 0)$ m and (d) $(0, 2000, 0)$ m as a function of the receiver along the y -direction at $x = 0$ m.

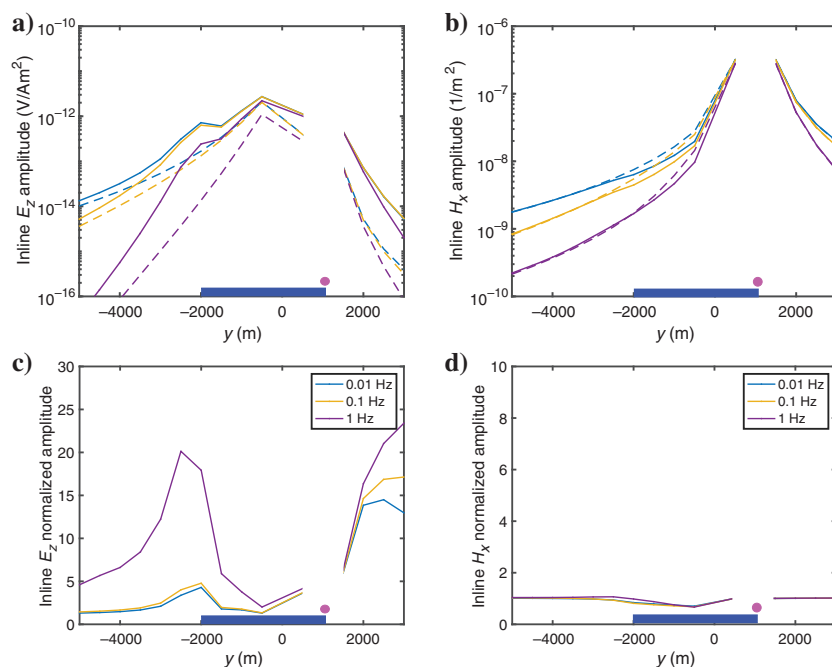


Figure 6. The same as Figure 4 except that the inline E_z and H_x are plotted. The (a) E_z amplitude and (b) H_x amplitude, and normalized amplitude (R^0) of (c) E_z and (d) H_x as a function of the receiver along the y -direction at $x = 0$ m. The transmitters at $(x, y, z) = (0, 1000, 0)$ m use a y -direction HED.

buried hydrocarbon reservoirs obtained similar results for the higher detectability of the inline electric field in comparison with the broadside electric field (Streich, 2016).

The sea depth in coastal areas ranges from a few meters to a few hundred meters. It is well known that there is a shallow-water air-wave problem in a marine CSEM. For shallow water (depths less than, e.g., 300 m), the airwave dominates the measured electromagnetic fields so that the sought-after signals from thin resistive bodies in the subsurface can be masked (Weiss, 2007; Constable, 2010; Løseth et al., 2010; Mittet and Morten, 2013). The sea depth may also affect the detectability of freshwater with our CSEM method. We investigated the effect of sea depth on the CSEM method's detectability of freshwater. Models with different sea depths ($d_1 = 10, 30$, and 100 m) but a fixed burial depth ($d_2 = 300$ m) were considered (Figure 2). The inline E_y generated from a y -direction transmitter dipole at $(0, 1000, 0)$ m exhibited a strong detectability for the three different sea depths (Figure 8). We note that the model with $d_1 = 30$ m is the same as that in Figure 3 that was used in the above tests. The maximum R^0 values at 1.0 Hz for $d_1 = 10, 30$, and 100 m were $3.0, 2.9$, and 2.5 , respectively. Although a d_1 of 100 m had a smaller peak R^0 value compared with those with a d_1 of 10 and 30 m, the detectability for $d_1 = 100$ m was still significant.

The depth of a buried target generally limits the detectability of CSEM methods. We conducted a test on the detectability of our CSEM method for different burial depths of freshwater. Models with different d_2 values ($100, 300$, and 1000 m) but a fixed d_1 of 30 m were considered (Figure 2). The results of the calculated inline E_y responses generated from a y -direction transmitter dipole at $(0, 1000, 0)$ m are shown in Figure 9. The peak R^0 value was $5.8, 2.8$, and 1.4 for a d_2 burial depth of $100, 300$, and 1000 m obtained at $1.0, 1.0$, and 0.1 Hz, respectively. Thus, the detectability of the shallower target was higher than that of the deeper target owing to the diffusive nature of the electromagnetic method.

The model of Figure 3 considers a freshwater body that is 3000 m long (-2000 to 1000 m on the y -axis). However, there is offshore freshwater more than tens of kilometers long (Gustafson et al., 2019). Knowing how far offshore our CSEM method can detect the freshwater helps us discuss the more general utility of the method. To study how far offshore our CSEM method can detect freshwater, we considered a model with a freshwater zone of 50 km in length (-25 to 25 km on the y -axis). The model includes 1 ohm-m sediments, 0.3 ohm-m seawater, and a

20 ohm-m freshwater zone. The freshwater dimensions are 2000 m (width) \times 50 km (length) \times 100 m (height) (Figure 10a). An air layer with resistivity of 10^8 ohm-m is present at the top of the model. The sea depth (d_1) is 30 m, and the freshwater burial depth (d_2) is 300 m. We generated CSEM responses from the model using forward modeling. A computation grid consisted of $56 \times 133 \times 95$ cells, including several boundary cells. For the horizontal cells, a 300 m grid was used.

We first considered an onshore transmitter at (0 m, 1 km, 0 m) for this detectability test. The transmitter used a y-direction HED. The transmitting frequencies were 0.01, 0.1, and 1.0 Hz. Receivers were deployed on the seafloor and ground at 1 km intervals from $y = -20$ to 20 km at a profile of $x = 0$ m. The inline E_y from a transmitter dipole at (0 m, 1 km, 0 m) showed the clear detectability of the target freshwater (Figure 10c and 10f). The high E_y amplitude ($R^0 > 1.2$) was observed at receivers of -5 to 7 km locations. This result implies that, if we use an onshore transmitter located near the shoreline, the resolvable range of offshore freshwater can be 5 km from the shoreline.

To detect freshwater on further offshore and onshore sides, we considered an offshore transmitter at $(x, y, z) = (0 \text{ m}, -10 \text{ km}, 30 \text{ m})$ and an onshore transmitter at (0 m, 10 km, 0 m). The inline E_y from a y-direction transmitter dipole at (0 m, -10 km , 30 m) detected the offshore freshwater away from the shoreline (Figure 10b and 10e). The high E_y amplitude ($R^0 > 1.2$) was observed at receivers of -16 to -4 km locations. The inline E_y from a y-direction transmitter dipole at (0 m, 10 km, 0 m) detected the onshore freshwater away from the shoreline (Figure 10d and 10g). The high E_y amplitude ($R^0 > 1.2$) was observed at receivers of 4 – 16 km locations. This result showed that offshore-onshore transmitters and receivers away from the shoreline are effective in detecting freshwater on further offshore and onshore sides. This test result also implies that the transmitter located at 6 km intervals from $y = -25$ to 25 km are necessary for resolving the whole extension of the freshwater.

Imaging ability using inversion

Inversion can convert the observed CSEM data to earth resistivity structures. We investigated the 3D CSEM inversion ability to image freshwater zones in coastal areas using the synthetic model shown in Figure 3 ($d_1 = 30 \text{ m}$; $d_2 = 300 \text{ m}$). Three onshore transmitter sites were located at $(x, y, z) = (0 \text{ m}, 1000 \text{ m}, 0 \text{ m})$, (0 m, 2000 m, 0 m), and (0 m, 3000 m, 0 m). Each transmitter site includes two HEDs oriented along the x- and y-directions. Receivers were deployed on the seafloor and ground at 500 m intervals from $y = -5000$ to 3000 m at three profiles of $x = -1500 \text{ m}$, 0 m, and 1500 m. The electromagnetic components (E_x , E_y , H_x , and H_y) for source-receiver distances greater than 500 m at frequencies of 0.05, 0.3, and 1 Hz resulted in an N of 5616. Vertical electric and magnetic fields were excluded because vertical field measurements are practically difficult in coastal areas due to sea waves. The input data used a combination of log10-scaled amplitude and linear-scaled phase of electromagnetic components due to the higher convergence in the inversion iteration (Wheelock et al., 2015).

We generated synthetic data from the true resistivity model in Figure 3 using forward modeling. The data were contaminated with 3% Gaussian random noise to provide a realistic inversion test. An error bar of 3% was set for all data. We applied a 3D data-space Occam inversion code to the synthetic data. The computation grid

for generating the synthetic data and performing the inversion consisted of $56 \times 133 \times 95$ cells. The grid was the same as that used in the aforementioned forward-modeling test. The starting and prior models for the inversion included a highly resistive air layer (10^8 ohm-m), a seawater layer of constant resistivity (0.3 ohm-m), and a homogeneous background (1 ohm-m). The inversion domain was limited to the region of interest and it excluded sea, air, and boundary cells, thus resulting in 306,816 unknown model parameters (i.e., M).

The initial root-mean-square (rms) misfit for the starting model was 3.3. After three iterations in Occam's phase I, the inversion reached the target rms misfit of 1.0, which indicates that the averaged misfit was within the assumed error level. Then, a further iteration was conducted to obtain the smoothest model with the target rms misfit in Occam's phase II. The inversion sufficiently recovered the positions and resistivity values of freshwater (Figure 11). The freshwater structure was distinguishable from 1 ohm-m sediments. The horizontal shapes of the recovered freshwater were close to those of the true model, as were the top and bottom of the recovered freshwater. However, the conductive artifacts appeared above and below the resistive target owing to the inversion's smoothness constraint and limited resolution of the CSEM data at depth.

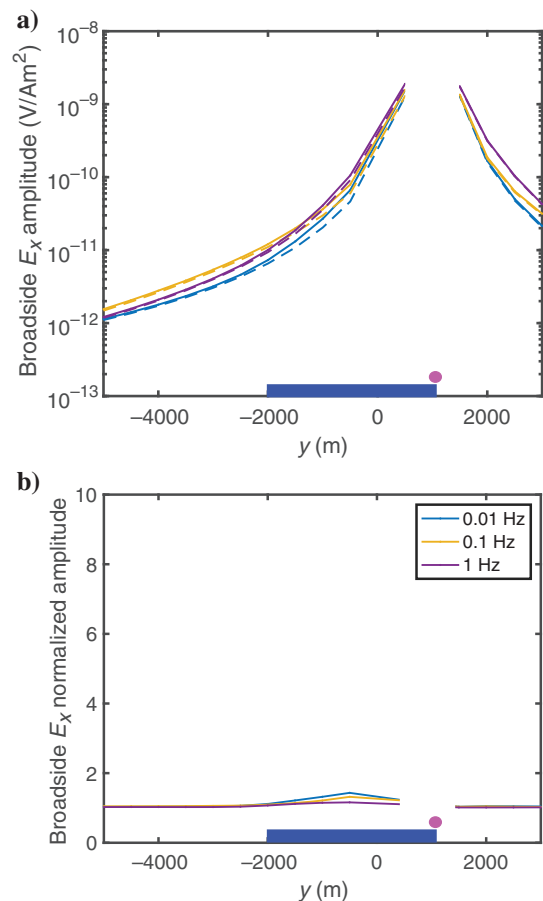


Figure 7. The same as Figure 4 except that the transmitter at $(x, y, z) = (0 \text{ m}, 1000 \text{ m}, 0 \text{ m})$ uses an x-direction HED and broadside E_x is plotted. (a) E_x amplitude and (b) The E_x normalized amplitude (R^0) as a function of the receiver along the y -direction at $x = 0$ m.

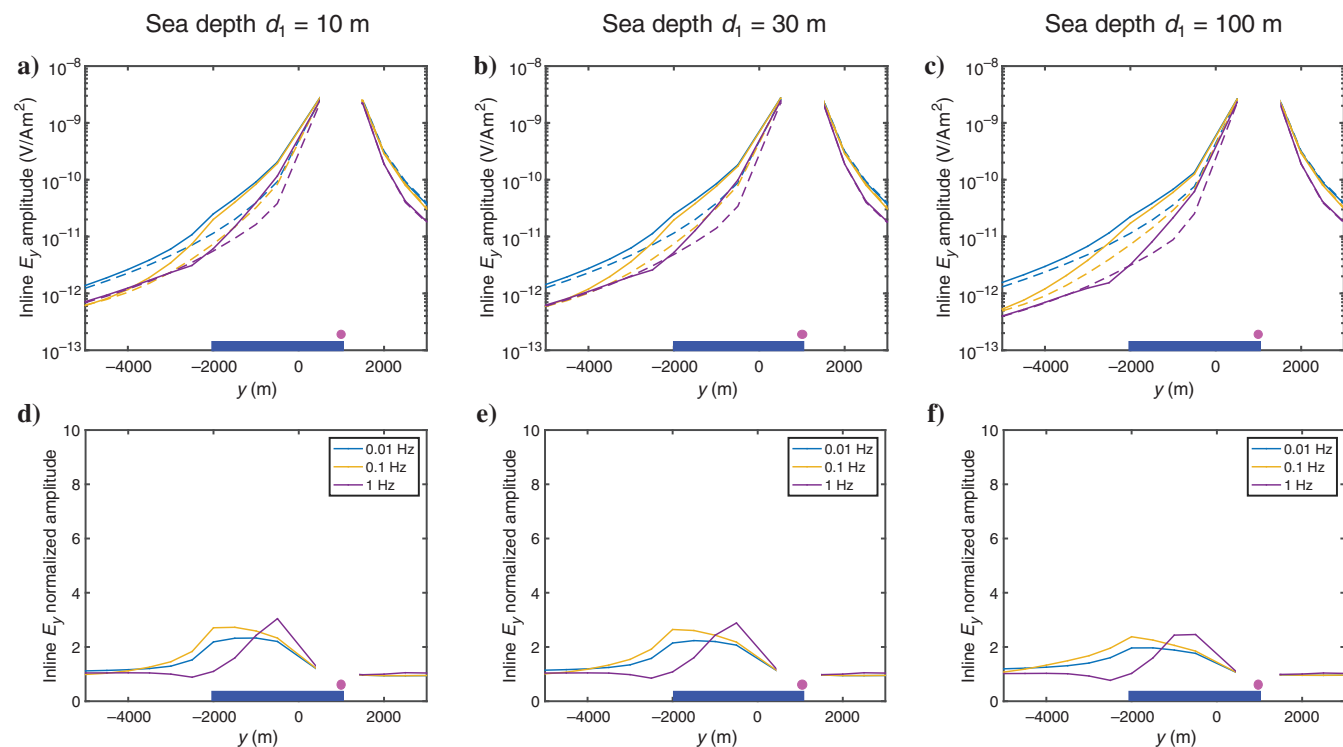


Figure 8. The same as Figure 4 except that in-line E_y amplitude and normalized amplitude are plotted for different sea depths (d_1) for the model shown in Figure 2 with the burial depth of freshwater (d_2) set to 300 m. The E_y amplitude for a sea depth (d_1) of (a) 10 m, (b) 30 m, and (c) 100 m as a function of the receiver along the y -direction at $x = 0$ m. The E_y normalized amplitude (R^0) for (d) $d_1 = 10$ m, (e) $d_1 = 30$ m, and (f) $d_1 = 100$ m. The transmitters at $(x, y, z) = (0 \text{ m}, 1000 \text{ m}, 0 \text{ m})$ use a y -direction HED.

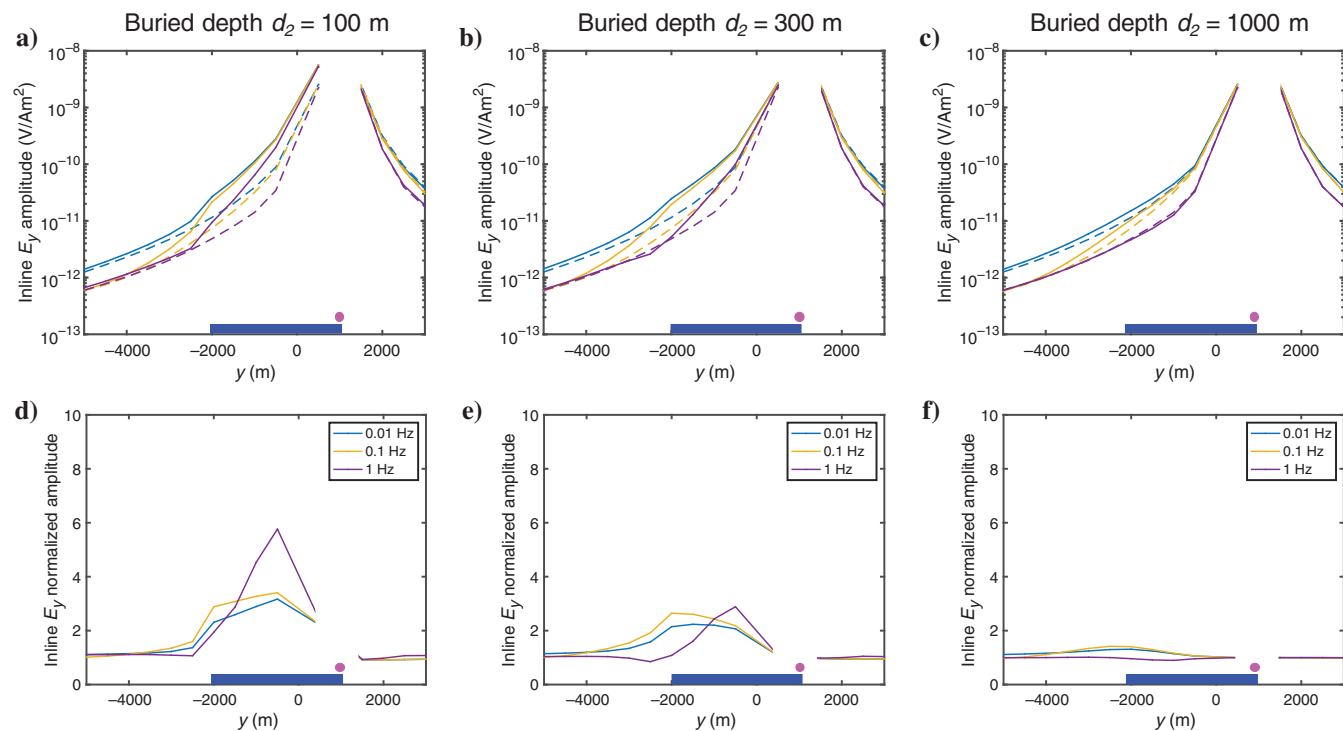


Figure 9. The same as Figure 4 except that in-line E_y amplitude and normalized amplitude are plotted for different freshwater burial depths (d_2) for the model shown in Figure 2 with the sea depth (d_1) set to 30 m. The E_y amplitude for a burial depth (d_2) of (a) 100 m, (b) 300 m, and (c) 1000 m as a function of the receiver along the y -direction at $x = 0$ m. The E_y normalized amplitude (R^0) for (d) $d_2 = 100$ m, (e) $d_2 = 300$ m, and (f) $d_2 = 1000$ m. The transmitters at $(x, y, z) = (0 \text{ m}, 1000 \text{ m}, 0 \text{ m})$ use a y -direction HED.

The forward-modeling test showed that the detectability of the CSEM method to the buried freshwater decreased with the increasing depth of the freshwater. Hence, we investigated the CSEM inversion's ability to map freshwater at different burial depths. We applied the inversion to synthetic data generated from the models in Figure 2 with $d_2 = 500$ and 1000 m ($d_1 = 30$ m). Similar to the inversion test with d_2 set to 300 m, we created synthetic data by adding 3% Gaussian noise to the true model's responses. The survey geometry was also the same as the test using $d_2 = 300$ m.

The initial rms misfit for the starting model was 2.8 and 1.6 for $d_2 = 500$ and 1000 m, respectively. The inversion reached a target misfit of 1.0 for both of these burial depths. The inversion could image freshwater clearly for $d_2 = 500$ m (Figure 12b). The anomaly structure was distinguishable from the 1 ohm-m sediments at a resolution that was similar to that for $d_2 = 300$ m. However, the freshwater was imaged at a shallower depth than that of the true model. The imaged anomaly structure is distinguishable from the 1 ohm-m sediments for $d_2 = 1000$ m (Figure 12c). However, the positions and resistivity values of the imaged freshwater were different from those of the true model because of their limited resolution to the deeply buried thin resistor. The results demonstrate that

the inversion of the CSEM method could be used to map freshwater buried at 500 m below the seafloor.

We considered 1 ohm-m resistivity for onshore and offshore parts in the preceding tests (Figures 2–12). However, the resistivity of 10–50 ohm-m is general for actual onshore sections (Goldman et al., 2011; Ueda et al., 2014; Haroon et al., 2017; Pedersen et al., 2017). Therefore, to consider a realistic coastal model, we set the onshore section to 10 ohm-m (Figure 13a). The freshwater resistivity is set to 100 ohm-m, and 1 ohm-m is used for the seafloor. The onshore side below the freshwater is set to 1 ohm-m. These resistivity values were derived from previously revealed coastal models (Goldman et al., 2011; Ueda et al., 2014; Haroon et al., 2017; Pedersen et al., 2017). The freshwater dimensions are 2000 m (width) \times 3000 m (length) \times 100 m (height) (Figure 13a). The geometry of the seawater and freshwater is the same as the model in Figure 3. An air layer with resistivity of 10^8 ohm-m is present at the top of the model. Similar to the previous inversion test, we created synthetic data by adding the 3% Gaussian noise to the true model's responses. The survey geometry was also the same as the test in Figure 3. We applied the inversion to synthetic data generated from the model in Figure 13a. For the initial and prior model, we used a two-layer

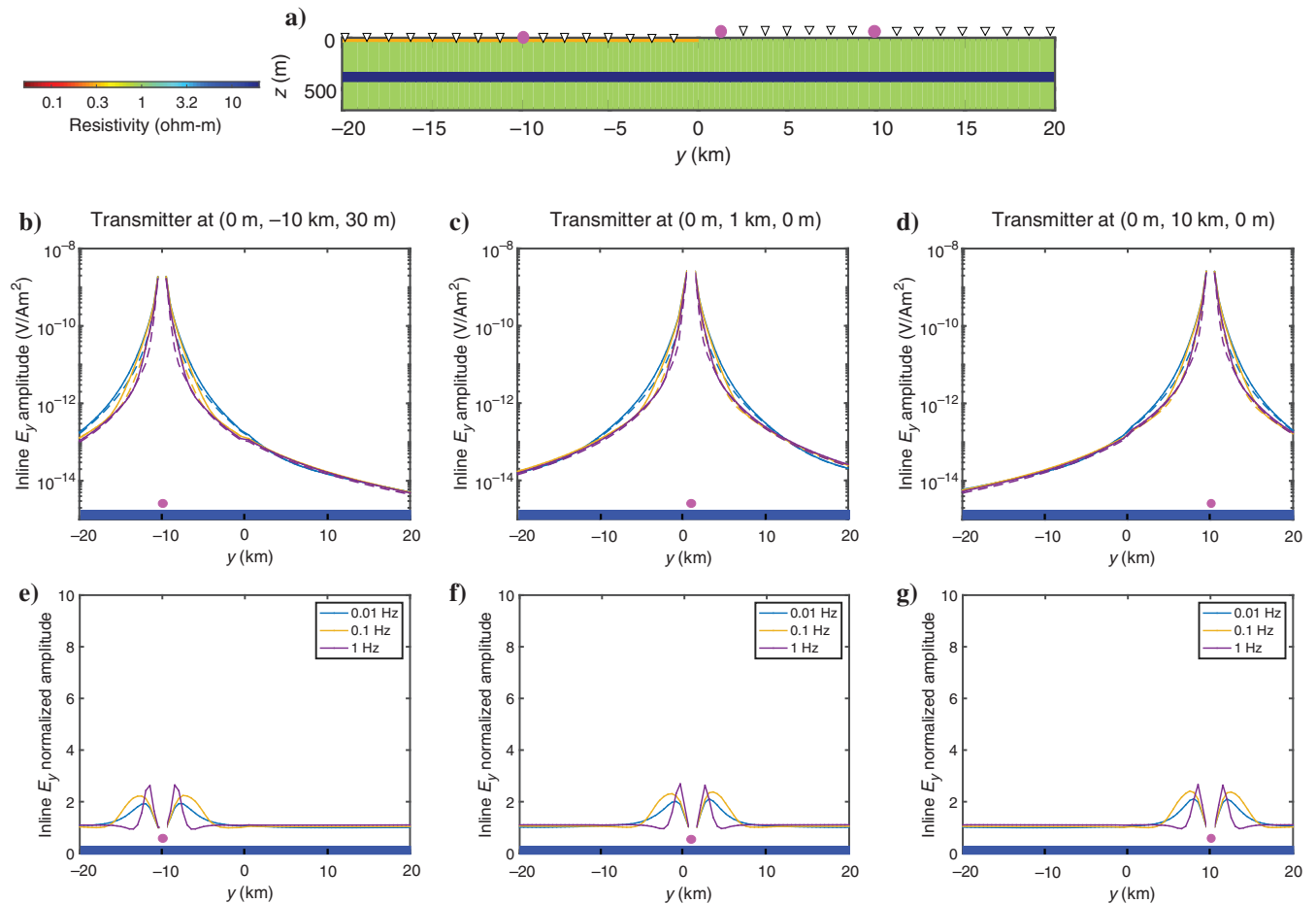


Figure 10. Detectability test for a freshwater zone with dimensions of 2000 m (width) \times 50 km (length) \times 100 m (height). (a) The 2D section of the test model at $x = 0$ m. The sea depth (d_1) is 30 m, and the freshwater burial depth (d_2) is 300 m. The E_y amplitude for the transmitter at (b) $(x, y, z) = (0 \text{ m}, -10 \text{ km}, 30 \text{ m})$, (c) $(0 \text{ m}, 1 \text{ km}, 0 \text{ m})$, and (d) $(0 \text{ m}, 10 \text{ km}, 0 \text{ m})$ as a function of the receiver along the y -direction at $x = 0$ m. The E_y normalized amplitude (R^0) for the transmitter at (e) $(x, y, z) = (0 \text{ m}, -10 \text{ km}, 30 \text{ m})$, (f) $(0 \text{ m}, 1 \text{ km}, 0 \text{ m})$, and (g) $(0 \text{ m}, 10 \text{ km}, 0 \text{ m})$. The circles and triangles show the transmitter and receiver positions, respectively. The transmitters use a y -direction HED.

resistivity of 10 and 1 ohm-m for offshore and onshore, respectively (Figure 13b).

The initial rms misfit for the starting model was 20.3. The inversion obtained the smoothest model with the target rms misfit after eight iterations. The imaged freshwater was distinguishable from 1 ohm-m sediments and 10 ohm-m onshore section (Figure 13c). The recovered geometry of the freshwater is close to the true one. The resistivity of the recovered freshwater is 70–90 ohm-m. The inversion also recovered the 1 ohm-m zone below the 10 ohm-m onshore section. The test result demonstrates that the proposed CSEM method is useful for mapping freshwater in a realistic coastal model. We conducted an inversion test with a different initial model to see the initial model effects on the inversion result. The inversion with the 1 ohm-m initial model also recovered the freshwater. Although the influence of the initial model on the final result is not significant, we found that the inversion with the initial model in Figure 13b had slightly better resolved the freshwater.

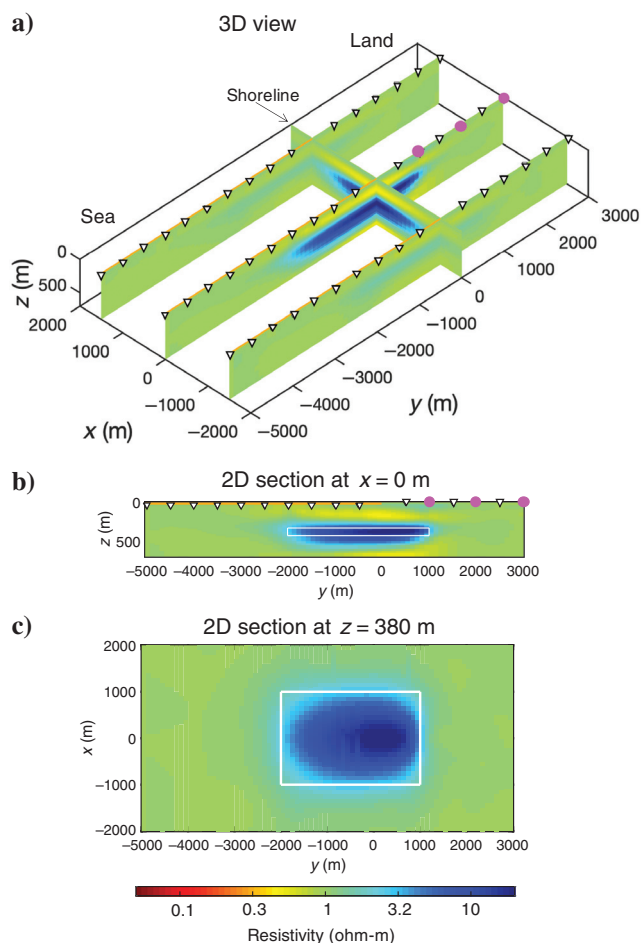


Figure 11. (a) The 3D view of the inversion results for the synthetic data generated from the model shown in Figure 3. The sea depth (d_1) is 30 m, and the freshwater burial depth (d_2) is 300 m. The circles and triangles show the transmitter and receiver positions, respectively. The 2D sections of the inverted resistivity model at (b) $x = 0$ m and (c) $z = 380$ m. The white lines mark the outlines of the true anomaly. The shoreline followed the x -direction at $y = 0$ m.

Comparison to the MT method

We compared the ability of CSEM inversion to image freshwater zones in coastal areas with MT inversion. The synthetic model used in this MT inversion test was the same as that used in the previous CSEM inversion test (Figure 3). As in the CSEM test, 48 receivers were deployed on the seafloor and ground. We generated synthetic MT data from the true resistivity model in Figure 3 using forward modeling of WSINV3DMT (Siripunvaraporn and Egbert, 2009). The synthetic data included the complex impedance tensor (Z_{xx} , Z_{xy} , Z_{yx} , and Z_{yy}) for 16 frequencies (0.001–1000 Hz) at 48 sites, thus resulting in an N of 6144. The data were contaminated with 3% Gaussian random noise to provide a realistic inversion test. An error bar of $3\% |Z_{xy}Z_{yx}|^{1/2}$ was set for all of the data. We applied a 3D inversion code WSINV3DMT (Siripunvaraporn and Egbert, 2009) to the synthetic data. The computation grid for generating synthetic data and performing the inversion consisted of $41 \times 65 \times 62$ cells. The horizontal mesh size was 250 m in the area near the observation sites, and it logarithmically increased with increasing distance from the observation sites. Between 0 and 1000 m, we set the vertical mesh size to values ranging from 1 to 150 m. For depths of less than 1000 m, the mesh size was increased with the increasing depth.

The starting and prior models for the inversion comprised a highly resistive air layer, seawater layer, and homogeneous background (1.2 ohm-m). The inversion domain was limited to the region of interest, and it excluded sea and air, thus resulting in 134,400 unknown model parameters (i.e., M). The initial rms misfit for the starting model was 1.9. The inversion produced the 3D resistivity model with an rms misfit of 0.96 after one iteration

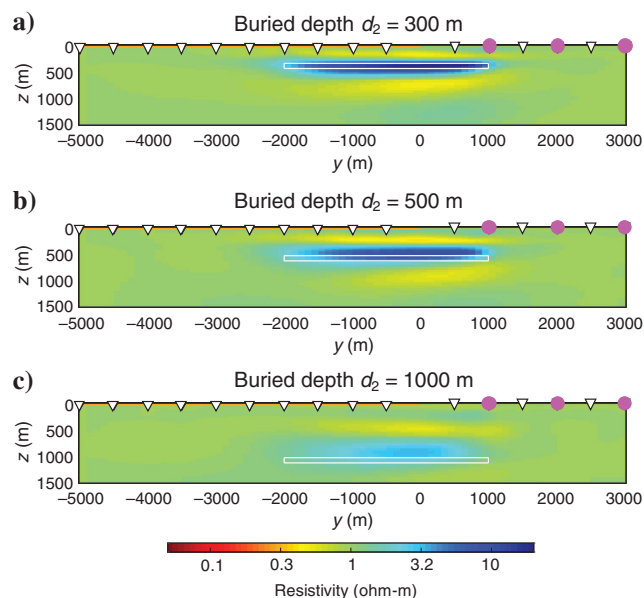


Figure 12. Inversion results for different freshwater burial depths. The 2D sections of the inversion results at $x = 0$ m are for a burial depth (d_2) of (a) 300 m, (b) 500 m, and (c) 1000 m. The tops of the buried freshwater for (a-c) are at $z = 330$ m, $z = 530$ m, and $z = 1030$ m, respectively. The sea depth (d_1) is 30 m in the three examples. (a) The same result as Figure 11b but with a different vertical range for comparison. The circles and triangles show the transmitter and receiver positions, respectively. The white lines mark the outlines of the true anomaly. The shoreline followed the x -direction at $y = 0$ m.

(Figure 14). The freshwater structure was hardly distinguishable from 1 ohm-m sediments. The shapes and resistivity values of the recovered freshwater differed from those of the true model. The inversion result comparison between the CSEM and MT methods revealed that the CSEM method had a better ability to map freshwater than the MT method (Figure 14).

DISCUSSION

The numerical tests showed that the inline electric field was sensitive to freshwater. We used the Poynting vector to explain the sensitivity to freshwater. The Poynting vector (W/m^2) can visualize the time-averaged energy flux in the earth resistivity structures (Chave, 2009), and it is expressed as follows:

$$\bar{\mathbf{S}} = \frac{1}{2} \text{Re}(\mathbf{E} \times \mathbf{H}^*) \quad (10)$$

where * denotes the complex conjugation. Figure 15 shows the real part of the complex Poynting vector for the model in Figure 3. The transmitter at $(x, y, z) = (0 \text{ m}, 1000 \text{ m}, 0 \text{ m})$ used a y -direction HED at a source frequency of 1.0 Hz. The Poynting vectors indicate that freshwater guided the electromagnetic energy along its length, which was due to the conservation of normal current flowing across its boundaries (Um and Alumbaugh, 2007; Key, 2012; Everett and Chave, 2019). As a result, the electric field was amplified on the seafloor receiver (Figures 4–10). Numerous studies have used CSEM methods to explore buried hydrocarbons with galvanic mechanisms (Eidesmo et al., 2002; Constable, 2010; Mittet and Morten, 2013; Zhdanov et al., 2014).

Inline geometry using the vertical and horizontal electric currents is much more sensitive to resistive freshwater than broadside geometry using the horizontal current (Figures 4 and 7). The Poynting vector revealed that the high detectability was caused by the galvanic effect of the vertical electric current across the buried freshwater. The existence of a vertical electric current amplified the inline E_y and E_z . However, broadside data primarily use inductive effects with a large horizontal current. Due to the sensitivity difference, a combination of inline and broadside data can improve the constraining of different resistivity structures (Constable, 2010). It is necessary to have a transmitter dipole oriented perpendicular and parallel to the shoreline to collect inline and broadside data in the field.

The numerical results showed that the CSEM responses in the near-field have a higher sensitivity to the thin buried resistor than in the far-field. The electromagnetic field can be treated as a plane wave in an area of a large transmitter-receiver distance (Garcia et al., 2003). This implies that the inline CSEM responses in the near-field area have a higher sensitivity to the thin buried resistor than MT methods using a plane-wave source. The sensitivity difference between the CSEM and MT methods is supported by the inversion test results (Figure 14). Although the MT data have low sensitivity to the thin buried resistor, they have deeper penetration than the CSEM method and are suitable for

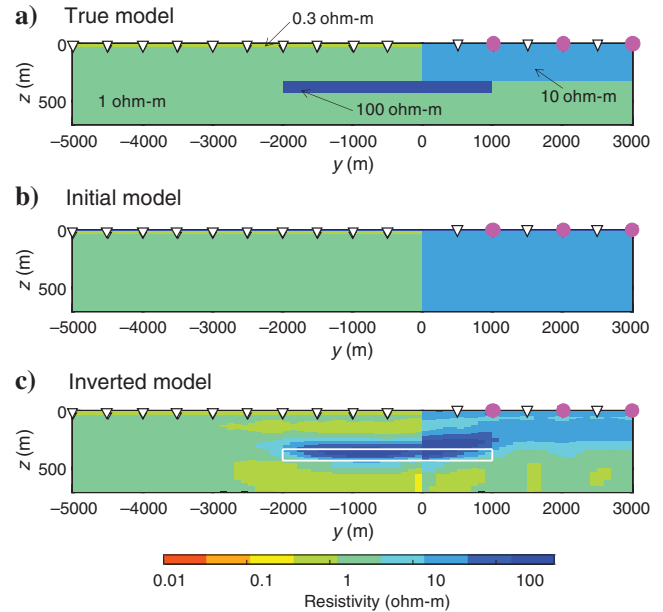


Figure 13. Inversion result for a model with 10 ohm-m onshore portion. The 2D sections at $x = 0 \text{ m}$ of the (a) true model, (b) initial model, and (c) inverted model. The true model includes 10 ohm-m onshore portion at a depth of 0–330 m. A 100 ohm-m freshwater reservoir (dimensions: 2000 m [width] \times 3000 m [length] \times 100 m [height]) is embedded into 1 ohm-m sediments (the top at $z = 330 \text{ m}$). The sea depth (d_1) is 30 m, and the freshwater burial depth (d_2) is 300 m. The initial model consists of the sea, 1 ohm-m offshore section, and 10 ohm-m onshore section. The circles and triangles show the transmitter and receiver positions, respectively. The white lines mark the outlines of the true anomaly. The shoreline followed the x -direction at $y = 0 \text{ m}$.

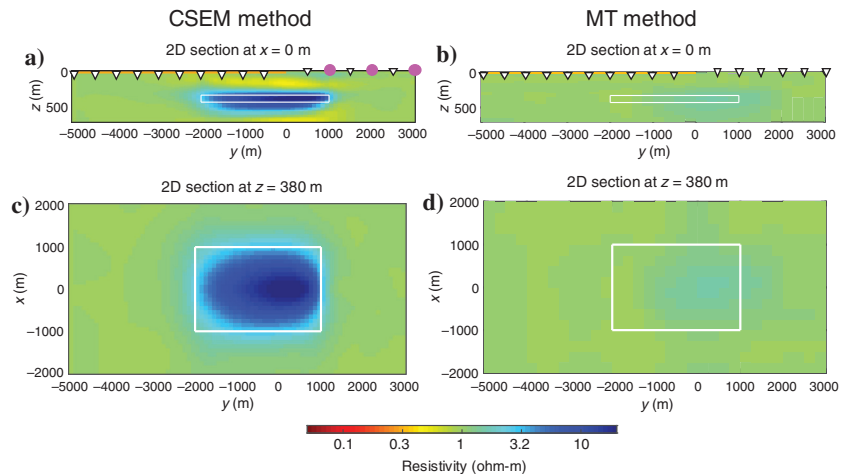


Figure 14. A comparison of CSEM and MT inversions for the model shown in Figure 3. The sea depth (d_1) is 30 m, and the freshwater burial depth (d_2) is 300 m. The 2D sections of the inversion results at (a) $x = 0 \text{ m}$ for CSEM, (b) $x = 0 \text{ m}$ for MT, (c) $z = 380 \text{ m}$ for CSEM, and (d) $z = 380 \text{ m}$ for MT. (a and c) The same results as shown in Figure 11b and 11c. The triangles and circles indicate the positions of the receivers and CSEM transmitters, respectively. The white lines mark the outlines of the true anomaly. The shoreline followed the x -direction at $y = 0 \text{ m}$.

determining large-scale structures. For example, we consider a two-layered structure in which the structure beneath the ground-water is deeper than the sensitivity of the CSEM data. The MT data are useful in constraining that deeper structure and, as a result, improving the ability of CSEM data to constrain the groundwater layer (Gustafson et al., 2019). This result indicates that the addition of MT data to CSEM data can be useful for imaging freshwater. The MT data can be measured simultaneously with CSEM data (Constable, 2013).

The vertical electric field showed a high detectability in freshwater (Figure 6). The high sensitivity of the vertical electric field to buried resistors has been shown in other modeling studies (Wirianto et al., 2010; Key, 2012; Streich, 2016) and in field surveys (Tietze et al., 2015; Constable et al., 2019). The amplitude of the vertical electric field is much smaller than the horizontal electric field (Figures 4 and 6). Moreover, measuring the vertical electric field is much more difficult than the horizontal electric field in practice for onshore and offshore environments. Due to the two reasons, we excluded the vertical field from the input data for the inversion test. Although we excluded the vertical electric field data for the inversion test, inversion of synthetic data without a vertical electric field could delineate freshwater (Figure 11).

We describe practical considerations of whether measuring data of sufficient quality is feasible and what instrument specifications are needed to obtain data of sufficient quality. We can convert the noise floor power P_n (V²/Hz) to a noise floor E_n (V/Am²) for the source dipole moment D (Am), receiver dipole length L (m), and a stacking window t_s (s) as follows (Constable, 2013):

$$E_n = \frac{\sqrt{P_n}}{DL\sqrt{t_s}}. \quad (11)$$

Marine electromagnetic receiver noise levels are approximately 10^{-9} V/ $\sqrt{\text{Hz}}$ at 1 Hz in deep water (based on Figure 6 in Constable, 2013). Measuring the 10^{-13} V/Am² signal at the seaward edge of the freshwater with 1% uncertainty requires $E_n = 10^{-15}$ V/Am² noise level. If we consider $\sqrt{P_n} = 10^{-9}$ V/ $\sqrt{\text{Hz}}$ at 1 Hz, $D = 5000$ Am dipole moment (a dipole length is 1000 m, and an output current is 5 A), and a $L = 10$ m receiver, $E_n = 10^{-15}$ V/Am² is possible with stacking for $t_s = 20^2$ s using equation 11. These measurements with $D = 5000$ Am dipole moment and $t_s = 20^2$ s stack length are feasible in field data

acquisitions. Note that a 10^{-15} V/Am² data error level could also be obtained with another combination of dipole moment and square-root stack length whose product equals 10^5 .

For shallow sea environments in coastal areas, the electromagnetic field at a frequency of 0.01–1 Hz is subject to motion noise caused by sea waves (Connell and Key, 2013; Ueda et al., 2014; Gustafson et al., 2019), and our model study showed that the frequency range is essential for freshwater imaging in coastal areas. For the higher noise level in shallow water, Figure 4 in Connell and Key (2013) shows that it is approximately 10 times noisier than the deepwater noise level in Constable (2013). If we assume a larger noise level of noise floor power $\sqrt{P_n} = 10^{-8}$ V/ $\sqrt{\text{Hz}}$ at 1 Hz for shallow sea environments and a $L = 10$ m receiver, measuring the 10^{-13} V/Am² signal with $E_n = 10^{-15}$ V/Am² noise level requires $D = 5000$ Am and stacking $t_s = 200^2$ s based on equation 11. Stacking data for 200² s (11 h) is a relatively easy requirement compared to the time required to install the transmitters and deploy the electromagnetic receiver arrays onshore and offshore. Therefore, we conclude that measurements of CSEM data of sufficient quality are feasible in a coastal area. Note that the lower frequency CSEM data (e.g., 0.01 Hz) will be limited by the MT noise. The MT noise is more than one order of magnitude larger at 0.01 than 1 Hz, as shown in Figure 4 in Connell and Key (2013) and Figure 6 in Constable (2013). The lower frequencies will require a bigger product of dipole moment and square-root stack length to overcome this MT noise.

The sea depth in coastal areas ranges from a few meters to a few hundred meters. The model test results exhibited high detectability at all sea depths from 10 to 100 m (Figure 8). The small effects of different sea depths on the level of detectability suggest that the CSEM method is applicable for freshwater exploration in most coastal areas. Ito et al. (2011) use an airborne TEM system with a grounded electrical dipole source and helicopter-towed magnetic field receiver to perform resistivity mapping in a coastal area. The penetration depth can be 300–350 m where shallow (approximately 5 m depth) water prevails. However, the detectability of resistivity structures below the seafloor is strongly limited in deep-sea regions. On the other hand, the proposed CSEM method offers the advantage of sea depth having little effect on detectability.

A high detectability of the freshwater was observed when the transmitter was located near the freshwater edge (Figure 4). Therefore, the transmitter should be located close to the shoreline to increase the detectability of offshore freshwater. If

we consider three onshore transmitters near the shoreline (Figure 3), our CSEM method can cover as far as 5 km offshore and 8 km onshore from the shoreline, respectively (Figure 10). If one needs to extend the survey area to the onshore and offshore sides, adding offshore-onshore transmitters and receivers away from the shoreline is necessary (Figure 10). However, we focus on the coastal region near the shoreline in this study. This CSEM method can cover as far as 5 km offshore from the shoreline. Hence, we assert that this CSEM method will be useful for studying various coastal areas.

Inversion test results using synthetic data revealed that the 3D inversion is useful for offshore-onshore resistivity imaging of freshwater

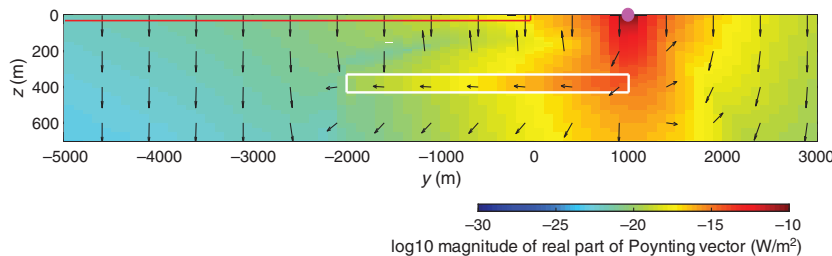


Figure 15. Contour plot of the logarithms (base 10) of the magnitude of the Poynting vector for the model shown in Figure 3 at 1.0 Hz. The sea depth (d_1) is 30 m, and the freshwater burial depth (d_2) is 300 m (top at $z = 330$ m). The transmitter uses a y-direction HED at $(x, y, z) = (0 \text{ m}, 1000 \text{ m}, 0 \text{ m})$. The Poynting vector plot also shows the energy flow direction. The arrow orientations were adjusted for the different horizontal and vertical scales. The magenta circle denotes the transmitter position. The white and red lines mark the outlines of the true anomaly and the seafloor, respectively. The shoreline followed the x -direction at $y = 0$ m.

(Figure 11). The inversion could map the thin freshwater buried at 500 m below the seafloor (Figure 12). Freshwater at the seafloor has been found at relatively shallow depths of a few hundred meters below the seafloor (Ueda et al., 2014; Blatter et al., 2019; Gustafson et al., 2019; Lippert and Tezkan, 2020; Micallef et al., 2020). The inversion test for a realistic coastal model with a 10 ohm-m onshore section showed that our method could map the freshwater below the 10 ohm-m onshore section (Figure 13). The results of the present study support the usefulness of the proposed CSEM method for freshwater exploration in real coastal areas. When freshwater was deeply buried in our model (the top of the freshwater being at 1000 m below the seafloor), the inversion poorly imaged the freshwater (Figure 12c). Incorporating borehole receiver data (Wilt et al., 1995; Hoversten et al., 2001; Kalscheuer et al., 2018) and prior information from logging data (Schaller et al., 2017) into the inversion process would improve the imaging ability for freshwater at depth.

There are conductive artifacts above and below the imaged freshwater due to the smoothness constraint and limited electromagnetic resolution at depth. Conductive artifacts also appeared in the smoothness inversion results for thin resistors (Oldenburg et al., 2005; Key, 2009). By relaxing the smoothing across the target boundary, the conductive artifacts disappeared and the resistor could be recovered close to the true model (Portniaguine and Zhdanov, 1999; Key, 2009; Brown et al., 2012). Information on boundaries to relax the smoothness is available from other geophysical data sets (e.g., seismic data and logging data). Conductive artifacts in coastal areas can be incorrectly interpreted as saltwater; hence, incorporating the adaptive smoothing technique into our inversion is essential for obtaining more accurate resistivity imaging.

The proposed CSEM method uses onshore transmitters. However, considering electromagnetic reciprocity in which the transmitter and receivers are exchangeable, seafloor transmitters have a similar detection for freshwater to that of land transmitters. Recent CSEM methods have used seafloor transmitters to explore offshore freshwater (Haroon et al., 2017; Gustafson et al., 2019; Lippert and Tezkan, 2020; Micallef et al., 2020). If seafloor transmitters are used, they can substitute the use of land transmitters for offshore-onshore resistivity imaging of freshwater. There are practical differences between onshore and offshore transmitters. Given the low resistivity of seawater, marine CSEM transmitters can have larger dipole moments than land transmitters. This is an advantage of using the marine transmitters for the proposed CSEM method. However, the survey cost with a marine CSEM transmitter is much higher than that with the land transmitter. The choice of land or marine transmitter for the proposed CSEM method depends on the survey cost and environment. If the freshwater extends further offshore, such as in the model in Figure 10, land and marine transmitters are needed to map the whole extension of the freshwater.

CONCLUSION

This study presents a CSEM modeling survey for offshore-onshore resistivity imaging of freshwater in a coastal area. Our CSEM method is novel in considering an array of onshore-offshore electromagnetic receivers with onshore electric dipole transmitters. We have conducted a feasibility study using 3D forward modeling and inversion to investigate our CSEM method's ability to map offshore-onshore resistivity structures of freshwater. The results show that this method could detect freshwater and that 3D inversion is

useful for offshore-onshore resistivity imaging of freshwater. The test results using forward modeling reveal that the offshore-onshore CSEM method can detect offshore aquifers up to 5 km from the shoreline, and the inline and vertical electric fields are sensitive to freshwater. The transmitter closest to the freshwater edge generates the highest detectability, which suggests that the transmitters should be located close to the shoreline for increasing the detectability of offshore freshwater. The detectability is sufficiently high at all sea depths from 10 to 100 m, which is a typical range for most coastal areas, thus indicating that this method can be used for coastal areas in general. Synthetic tests demonstrate that resistivity imaging using 3D inversion of CSEM data could map the thin layer of freshwater buried at 500 m below the seafloor. Based on our modeling results, we conclude that the proposed CSEM method is a promising technique for offshore-onshore resistivity imaging of freshwater in coastal areas. We plan to obtain field data using the CSEM method to validate its effectiveness in the real environment.

ACKNOWLEDGMENTS

Constructive comments by C. Farquharson, R. Evans, and K. Key led to significant improvements in the manuscript. We thank associate editor A. Abubakar and editor-in-chief J. Shragge for handling the submission. We also thank W. Siripunvaraporn for allowing us to use the MT inversion code. H. Kawamura and M. Yamakawa stimulated this study. This work was supported by the Japan Society for the Promotion of Science KAKENHI (grant no. 20K22326).

DATA AND MATERIALS AVAILABILITY

Data associated with this research are available and can be obtained by contacting the corresponding author.

REFERENCES

- Archie, G. E., 1942, The electrical resistivity log as an aid in determining some reservoir characteristics: *Transactions of the American Institute of Mining, Metallurgical, and Petroleum Engineers*, **146**, 54–62.
- Attias, E., D. Thomas, D. Sherman, K. Ismail, and S. Constable, 2020, Marine electrical imaging reveals novel freshwater transport mechanism in Hawai'i: *Science Advances*, **6**, eabd4866, doi: [10.1126/sciadv.abd4866](https://doi.org/10.1126/sciadv.abd4866).
- Binley, A., S. S. Hubbard, J. A. Huisman, A. Revil, D. A. Robinson, K. Singha, and L. D. Slater, 2015, The emergence of hydrogeophysics for improved understanding of subsurface processes over multiple scales: *Water Resources Research*, **51**, 3837–3866, doi: [10.1002/2015WR017016](https://doi.org/10.1002/2015WR017016).
- Blatter, D., K. Key, A. Ray, C. Gustafson, and R. Evans, 2019, Bayesian joint inversion of controlled source electromagnetic and magnetotelluric data to image freshwater aquifer offshore New Jersey: *Geophysical Journal International*, **218**, 1822–1837, doi: [10.1093/gji/ggz253](https://doi.org/10.1093/gji/ggz253).
- Brown, V., K. Key, and S. Singh, 2012, Seismically regularized controlled-source electromagnetic inversion: *Geophysics*, **77**, no. 1, E57–E65, doi: [10.1190/geo2011-0081.1](https://doi.org/10.1190/geo2011-0081.1).
- Caldwell, G., H. M. Bibby, and C. Brown, 2002, Controlled source apparent resistivity tensors and their relationship to the magnetotelluric impedance tensor: *Geophysical Journal International*, **151**, 755–770, doi: [10.1046/j.1365-246X.2002.01798.x](https://doi.org/10.1046/j.1365-246X.2002.01798.x).
- Chave, A. D., 2009, On the electromagnetic fields produced by marine frequency domain controlled sources: *Geophysical Journal International*, **179**, 1429–1457, doi: [10.1111/j.1365-246X.2009.04367.x](https://doi.org/10.1111/j.1365-246X.2009.04367.x).
- Commer, M., and G. A. Newman, 2009, Three-dimensional controlled-source electromagnetic and magnetotelluric joint inversion: *Geophysical Journal International*, **178**, 1305–1316, doi: [10.1111/j.1365-246X.2009.04216.x](https://doi.org/10.1111/j.1365-246X.2009.04216.x).
- Connell, D., and K. Key, 2013, A numerical comparison of time and frequency-domain marine electromagnetic methods for hydrocarbon

- exploration in shallow water: *Geophysical Prospecting*, **61**, 187–199, doi: [10.1111/j.1365-2478.2012.01037.x](https://doi.org/10.1111/j.1365-2478.2012.01037.x).
- Constable, S., 2010, Ten years of marine CSEM for hydrocarbon exploration: *Geophysics*, **75**, no. 5, 75A67–75A81, doi: [10.1190/1.3483451](https://doi.org/10.1190/1.3483451).
- Constable, S., 2013, Review paper: Instrumentation for marine magnetotelluric and controlled source electromagnetic sounding: *Geophysical Prospecting*, **61**, 505–532, doi: [10.1111/j.1365-2478.2012.01117.x](https://doi.org/10.1111/j.1365-2478.2012.01117.x).
- Constable, S., A. Orange, and D. Myer, 2019, Marine controlled-source electromagnetic of the Scarborough gas field — Part 3: Multicomponent 2D magnetotelluric/controlled-source electromagnetic inversions: *Geophysics*, **84**, no. 6, B387–B401, doi: [10.1190/geo2019-0314.1](https://doi.org/10.1190/geo2019-0314.1).
- Constable, S. C., R. L. Parker, and C. G. Constable, 1987, Occam's inversion: A practical algorithm for generating smooth models from electromagnetic sounding data: *Geophysics*, **52**, 289–300, doi: [10.1190/1.1442303](https://doi.org/10.1190/1.1442303).
- Dimova, N. T., P. W. Swarzenski, H. Dulaiova, and C. R. Glenn, 2012, Utilizing multichannel electrical resistivity methods to examine the dynamics of the fresh water–seawater interface in two Hawaiian groundwater systems: *Journal of Geophysical Research: Oceans*, **117**, C02012, doi: [10.1029/2011JC007509](https://doi.org/10.1029/2011JC007509).
- Eidesmo, T., S. Ellingsrud, L. M. MacGregor, S. Constable, M. C. Sinha, S. Johansen, F. N. Kong, and H. Westerdahl, 2002, Sea bed logging (SBL), a new method for remote and direct identification of hydrocarbon filled layers in deepwater areas: *First Break*, **20**, 144–152.
- Evans, R. L., 2007, Using CSEM techniques to map the shallow section of seafloor: From the coastline to the edges of the continental slope: *Geophysics*, **72**, no. 2, WA105–WA116, doi: [10.1190/1.2434798](https://doi.org/10.1190/1.2434798).
- Everett, M. E., and A. D. Chave, 2019, On the physical principles underlying electromagnetic induction: *Geophysics*, **84**, no. 5, W21–W32, doi: [10.1190/geo2018-0232.1](https://doi.org/10.1190/geo2018-0232.1).
- Garcia, X., D. Boerner, and L. B. Pedersen, 2003, Electric and magnetic galvanic distortion decomposition of tensor CSAMT data. Application to data from the Buchans Mine (Newfoundland, Canada): *Geophysical Journal International*, **154**, 957–969, doi: [10.1046/j.1365-246X.2003.02019.x](https://doi.org/10.1046/j.1365-246X.2003.02019.x).
- Gaus, I., 2010, Role and impact of CO₂–rock interactions during CO₂ storage in sedimentary rocks: *International Journal of Greenhouse Gas Control*, **4**, 73–89, doi: [10.1016/j.ijggc.2009.09.015](https://doi.org/10.1016/j.ijggc.2009.09.015).
- Goldman, M., E. Levi, B. Tezkan, and P. Yogeshwar, 2011, The 2D coastal effect on marine time domain electromagnetic measurements using broadband dBz/dt of an electrical transmitter dipole: *Geophysics*, **76**, no. 2, F101–F109, doi: [10.1190/1.3525276](https://doi.org/10.1190/1.3525276).
- Grayver, A. V., R. Streich, and O. Ritter, 2014, 3D inversion and resolution analysis of land-based CSEM data from the Ketzin CO₂ storage formation: *Geophysics*, **79**, no. 2, E101–E114, doi: [10.1190/geo2013-0184.1](https://doi.org/10.1190/geo2013-0184.1).
- Gustafson, C., K. Key, and R. L. Evans, 2019, Aquifer systems extending far offshore on the U.S. Atlantic margin: *Scientific Reports*, **9**, 8709, doi: [10.1038/s41598-019-44611-7](https://doi.org/10.1038/s41598-019-44611-7).
- Haroon, A., S. Hölz, R. A. Gehrmann, E. Attias, M. Jegen, T. A. Minshall, and B. J. Murton, 2018, Marine dipole–dipole controlled source electromagnetic and coincident-loop transient electromagnetic experiments to detect seafloor massive sulphides: Effects of three-dimensional bathymetry: *Geophysical Journal International*, **215**, 2156–2171, doi: [10.1093/gji/ggy398](https://doi.org/10.1093/gji/ggy398).
- Haroon, A., K. Lippert, V. Mogilatov, and B. Tezkan, 2017, First application of the marine differential electric dipole for groundwater investigations: A case study from Bat Yam, Israel: *Geophysics*, **83**, no. 2, B59–B76, doi: [10.1190/geo2017-0162.1](https://doi.org/10.1190/geo2017-0162.1).
- Hermans, T., and M. Paepen, 2020, Combined inversion of land and marine electrical resistivity tomography for submarine groundwater discharge and saltwater intrusion characterization: *Geophysical Research Letters*, **47**, e2019GL085877, doi: [10.1029/2019GL085877](https://doi.org/10.1029/2019GL085877).
- Hoversten, G. M., G. A. Newman, H. F. Morrison, E. Gasperikova, and J. Berg, 2001, Reservoir characterization using crosswell electromagnetic inversion: A feasibility study for the Snorre field, North Sea: *Geophysics*, **66**, 1177–1189, doi: [10.1190/1.1487064](https://doi.org/10.1190/1.1487064).
- Ito, H., T. Mogi, A. Jomori, Y. Yuuki, K. Kiho, H. Kaieda, K. Suzuki, K. Tsukuda, and S. A. Allah, 2011, Further investigations of underground resistivity structures in coastal areas using grounded-source airborne electromagnetics: *Earth, Planets and Space*, **63**, e9–e12, doi: [10.5047/eps.2011.08.003](https://doi.org/10.5047/eps.2011.08.003).
- Johansen, S. E., M. Panzner, R. Mittet, H. E. Amundsen, A. Lim, E. Vik, M. Landrø, and B. Arntsen, 2019, Deep electrical imaging of the ultraslow-spreading Mohs Ridge: *Nature*, **567**, 379–383, doi: [10.1038/s41586-019-1010-0](https://doi.org/10.1038/s41586-019-1010-0).
- Johnston, R. H., 1983, The saltwater–freshwater interface in the Tertiary limestone aquifer, southeast Atlantic outer-continental shelf of the USA: *Journal of Hydrology*, **61**, 239–249, doi: [10.1016/0022-1694\(83\)90251-2](https://doi.org/10.1016/0022-1694(83)90251-2).
- Kalscheuer, T., N. Juhojuntti, and K. Vaitinen, 2018, Two-dimensional magnetotelluric modelling of ore deposits: Improvements in model constraints by inclusion of borehole measurements: *Surveys in Geophysics*, **39**, 467–507, doi: [10.1007/s10712-017-9454-y](https://doi.org/10.1007/s10712-017-9454-y).
- Key, K., 2009, 1D inversion of multicomponent, multifrequency marine CSEM data: Methodology and synthetic studies for resolving thin resistive layers: *Geophysics*, **74**, no. 2, F9–F20, doi: [10.1190/1.3058434](https://doi.org/10.1190/1.3058434).
- Key, K., 2012, Marine electromagnetic studies of seafloor resources and tectonics: *Surveys in Geophysics*, **33**, 135–167, doi: [10.1007/s10712-011-9139-x](https://doi.org/10.1007/s10712-011-9139-x).
- Lippert, K., and B. Tezkan, 2020, On the exploration of a marine aquifer offshore Israel by long-offset transient electromagnetics: *Geophysical Prospecting*, **68**, 999–1015, doi: [10.1111/1365-2478.12875](https://doi.org/10.1111/1365-2478.12875).
- Løseth, L. O., L. Amundsen, and A. J. Jenssen, 2010, A solution to the air-wave-removal problem in shallow-water marine EM: *Geophysics*, **75**, no. 5, A37–A42, doi: [10.1190/1.3475359](https://doi.org/10.1190/1.3475359).
- Malovichko, M., A. V. Tarasov, N. Yavich, and M. S. Zhdanov, 2019, Mineral exploration with 3-D controlled-source electromagnetic method: A synthetic study of Sukhoi Log gold deposit: *Geophysical Journal International*, **219**, 1698–1716, doi: [10.1093/gji/ggz390](https://doi.org/10.1093/gji/ggz390).
- Micallef, A., M. Person, A. Haroon, B. A. Weymer, M. Jegen, K. Schwalenberg, Z. Faghghi, S. Duan, D. Cohen, J. J. Mountjoy, S. Woelz, C. W. Gable, T. Avers, and A. Kumar Tiwari, 2020, 3D characterisation and quantification of an offshore freshened groundwater system in the Canterbury Bight: *Nature Communications*, **11**, 1372, doi: [10.1038/s41467-020-14770-7](https://doi.org/10.1038/s41467-020-14770-7).
- Mitsuhata, Y., T. Uchida, K. Matsuo, A. Marui, and K. Kusunose, 2006, Various-scale electromagnetic investigations of high-salinity zones in a coastal plain: *Geophysics*, **71**, no. 6, B167–B173, doi: [10.1190/1.2335658](https://doi.org/10.1190/1.2335658).
- Mittet, R., and J. P. Morten, 2013, The marine controlled-source electromagnetic method in shallow water: *Geophysics*, **78**, no. 2, E67–E77, doi: [10.1190/geo2012-0112.1](https://doi.org/10.1190/geo2012-0112.1).
- Newman, G. A., and D. L. Alumbaugh, 1997, Three-dimensional massively parallel electromagnetic inversion — 1: Theory: *Geophysical Journal International*, **128**, 345–354, doi: [10.1111/j.1365-246X.1997.tb01559.x](https://doi.org/10.1111/j.1365-246X.1997.tb01559.x).
- Oldenburg, D., R. Eso, S. Napier, and E. Haber, 2005, Controlled source electromagnetic inversion for resource exploration: *First Break*, **23**, 7–78, doi: [10.3997/1365-2397.23.7.26611](https://doi.org/10.3997/1365-2397.23.7.26611).
- Oldenburg, D. W., E. Haber, and R. Shekhtman, 2013, Three dimensional inversion of multisource time domain electromagnetic data: *Geophysics*, **78**, no. 1, E47–E57, doi: [10.1190/geo2012-0131.1](https://doi.org/10.1190/geo2012-0131.1).
- Pedersen, J. B., F. W. Schaars, A. V. Christiansen, N. Foged, C. Schamper, H. Rolf, and E. Auken, 2017, Mapping the fresh-saltwater interface in the coastal zone using high-resolution airborne electromagnetics: *First Break*, **35**, 57–61, doi: [10.3997/1365-2397.35.8.89806](https://doi.org/10.3997/1365-2397.35.8.89806).
- Plessix, R.-É., and W. A. Mulder, 2008, Resistivity imaging with controlled-source electromagnetic data: Depth and data weighting: *Inverse Problems*, **24**, 034012, doi: [10.1088/0266-5611/24/3/034012](https://doi.org/10.1088/0266-5611/24/3/034012).
- Portnaguine, O., and M. S. Zhdanov, 1999, Focusing geophysical inversion images: *Geophysics*, **64**, 874–887, doi: [10.1190/1.1444596](https://doi.org/10.1190/1.1444596).
- Post, V. E. A., 2005, Fresh and saline groundwater interaction in coastal aquifers: Is our technology ready for the problems ahead?: *Hydrogeology Journal*, **13**, 120–123, doi: [10.1007/s10040-004-0417-2](https://doi.org/10.1007/s10040-004-0417-2).
- Revil, A., L. M. Cathles, III, S. Losh, and J. A. Nunn, 1998, Electrical conductivity in shaly sands with geophysical applications: *Journal of Geophysical Research: Solid Earth*, **103**, 23925–23936, doi: [10.1029/98JB02125](https://doi.org/10.1029/98JB02125).
- Sawada, Y., J. Tanaka, C. Suzuki, D. Tanase, and Y. Tanaka, 2018, Tomakomai CCS demonstration project of Japan, CO₂ injection in progress: *Applied Energy Symposium and Forum, Carbon Capture, Utilization and Storage, CCUS 2018* 154, 3–8.
- Schaller, A., R. Streich, G. Drijkoningen, O. Ritter, and E. Slob, 2017, A land-based controlled-source electromagnetic method for oil field exploration: An example from the Schoonebeek oil field: *Geophysics*, **83**, no. 2, WB1–WB17, doi: [10.1190/geo2017-0022.1](https://doi.org/10.1190/geo2017-0022.1).
- Schwalenberg, K., M. Haeckel, J. Poort, and M. Jegen, 2010, Evaluation of gas hydrate deposits in an active seep area using marine controlled source electromagnetics: Results from Opuawe Bank, Hikurangi Margin, New Zealand: *Marine Geology*, **272**, 79–88, doi: [10.1016/j.margeo.2009.07.006](https://doi.org/10.1016/j.margeo.2009.07.006).
- Sherman, D., P. Kannberg, and S. Constable, 2017, Surface towed electromagnetic system for mapping of subsea Arctic permafrost: *Earth and Planetary Science Letters*, **460**, 97–104, doi: [10.1016/j.epsl.2016.12.002](https://doi.org/10.1016/j.epsl.2016.12.002).
- Siripunvaraporn, W., and G. Egbert, 2000, An efficient data-subspace inversion method for 2-D magnetotelluric data: *Geophysics*, **65**, 791–803, doi: [10.1190/1.1444778](https://doi.org/10.1190/1.1444778).
- Siripunvaraporn, W., and G. Egbert, 2009, WSVIN3DMT: Vertical magnetic field transfer function inversion and parallel implementation: *Physics of the Earth and Planetary Interiors*, **173**, 317–329, doi: [10.1016/j.pepi.2009.01.013](https://doi.org/10.1016/j.pepi.2009.01.013).
- Strack, K. M., 2014, Future directions of electromagnetic methods for hydrocarbon applications: *Surveys in Geophysics*, **35**, 157–177, doi: [10.1007/s10712-013-9237-z](https://doi.org/10.1007/s10712-013-9237-z).

- Streich, R., 2016, Controlled-source electromagnetic approaches for hydrocarbon exploration and monitoring on land: *Surveys in Geophysics*, **37**, 47–80, doi: [10.1007/s10712-015-9336-0](https://doi.org/10.1007/s10712-015-9336-0).
- Suzuki, K., Y. Kusano, R. Ochi, N. Nishiyama, T. Tokunaga, and K. Tanaka, 2017, Electromagnetic exploration in high-salinity groundwater zones: Case studies from volcanic and soft sedimentary sites in coastal Japan: *Exploration Geophysics*, **48**, 95–109, doi: [10.1071/EG15121](https://doi.org/10.1071/EG15121).
- Swidinsky, A., R. N. Edwards, and M. Jegen, 2013, The marine controlled source electromagnetic response of a steel borehole casing: Applications for the NEPTUNE Canada gas hydrate observatory: *Geophysical Prospecting*, **61**, 842–856, doi: [10.1111/1365-2478.12007](https://doi.org/10.1111/1365-2478.12007).
- Tietze, K., O. Ritter, and P. Veeken, 2015, Controlled-source electromagnetic monitoring of reservoir oil saturation using a novel borehole-to-surface configuration: *Geophysical Prospecting*, **63**, 1468–1490, doi: [10.1111/1365-2478.12322](https://doi.org/10.1111/1365-2478.12322).
- Ueda, T., Y. Mitsuhashi, T. Uchida, A. Marui, and K. Ohsawa, 2014, A new marine magnetotelluric measurement system in a shallow-water environment for hydrogeological study: *Journal of Applied Geophysics*, **100**, 23–31, doi: [10.1016/j.jappgeo.2013.10.003](https://doi.org/10.1016/j.jappgeo.2013.10.003).
- Um, E. S., and D. L. Alumbaugh, 2007, On the physics of the marine controlled-source electromagnetic method: *Geophysics*, **72**, no. 2, WA13–WA26, doi: [10.1190/1.2432482](https://doi.org/10.1190/1.2432482).
- Weiss, C. J., 2007, The fallacy of the “shallow-water problem” in marine CSEM exploration: *Geophysics*, **72**, no. 6, A93–A97, doi: [10.1190/1.2786868](https://doi.org/10.1190/1.2786868).
- Weiss, C. J., and S. Constable, 2006, Mapping thin resistors and hydrocarbons with marine EM methods — Part 2: Modeling and analysis in 3D: *Geophysics*, **71**, no. 6, G321–G332, doi: [10.1190/1.2356908](https://doi.org/10.1190/1.2356908).
- Wheelock, B., S. Constable, and K. Key, 2015, The advantages of logarithmically scaled data for electromagnetic inversion: *Geophysical Journal International*, **201**, 1765–1780, doi: [10.1093/gji/ggv107](https://doi.org/10.1093/gji/ggv107).
- Wilt, M. J., D. L. Alumbaugh, H. F. Morrison, A. Becker, K. H. Lee, and M. Deszcz-Pan, 1995, Crosswell electromagnetic tomography: System design considerations and field results: *Geophysics*, **60**, 871–885, doi: [10.1190/1.1443823](https://doi.org/10.1190/1.1443823).
- Wirianto, M., W. A. Mulder, and E. C. Slob, 2010, A feasibility study of land CSEM reservoir monitoring in a complex 3-D model: *Geophysical Journal International*, **181**, 741–755.
- Zhdanov, M. S., M. Endo, D. Yoon, M. Čuma, J. Mattsson, and J. Midgley, 2014, Anisotropic 3D inversion of towed-streamer electromagnetic data: Case study from the Troll West Oil Province: *Interpretation*, **2**, no. 3, SH97–SH113, doi: [10.1190/INT-2013-0156.1](https://doi.org/10.1190/INT-2013-0156.1).

Biographies and photographs of the authors are not available.